TEM and XPS studies of nanocrystals and clusters in nanostructured materials used for memory storage applications

Annett Thøgersen

Thesis submitted in partial fulfillment
of the requirements for the degree of
Philosophiae Doctor

Department of Physics
University of Oslo

April 2009

© Annett Thøgersen, 2009

Series of dissertations submitted to the
Faculty of Mathematics and Natural Sciences, University of Oslo
Nr. 859

ISSN 1501-7710

All rights reserved. No part of this publication may be
reproduced or transmitted, in any form or by any means, without permission.

Cover: Inger Sandved Anfinsen.
Printed in Norway: AiT e-dit AS, Oslo, 2009.

Produced in co-operation with Unipub AS.
The thesis is produced by Unipub AS merely in connection with the
thesis defence. Kindly direct all inquiries regarding the thesis to the copyright
holder or the unit which grants the doctorate.

Unipub AS is owned by
The University Foundation for Student Life (SiO)

Summary

Nanoscaled electronic devices have attracted much attention due to their optical and electronic properties, especially related to MOS (Metal-Oxide-Semiconductor) devices used for memory storage applications. Improved electrical properties, longer retention, lower gate voltage and lower power consumption are assumed to be possible when replacing bulk floating gate in flash memory devices with nanocrystals. Multilayer samples with Si, Ge, Er-oxide, and Pd nanocrystals and clusters were studied in detail. The nucleation, distribution, defects, composition, and atomic and electronic structure are important factors to understand in order to improve performance of memory storage devices. These parameters were studied by high resolution transmission electron microscopy, energy filtered transmission electron microscopy, electron energy loss spectroscopy, X-ray photoelectron spectroscopy, energy dispersive spectroscopy, and secondary ion-mass spectrometry.

Acknowledgments

The past four years have been tough, crazy, and fun. There are many people I wish to thank for supporting and helping me with my PhD project and generally for keeping me sane.

First of all I want to thank Arne Olsen for supervising me and helping me with my work. You lured me into electron microscopy, supported me, and challenged me. This I will use in many years to come. Spyros Diplas, your knowledge of XPS altered the course of my thesis, paving the way for new results. But most of all you inspired me to view data from a different angle.

Furthermore, I wish to thank the administrators at the Department of Physics, SMN, and FUNMAT@UIO for funding and providing all the means for my project. I am grateful to Terje Finstad, Bengt Svensson, Jeyanthinath Mayandi, Lasse Vines, Jens Christensen, Martin F. Sunding, Anette Gunnæs, Johan Taftø, Ole Bjørn Karlsen, Mesanori Mitome, and Yoshio Bando for supporting my thesis work.

I also want to thank my friends, especially Bailey, Ingunn, Ingvild, Kanutte, Klaus, and Øystein for invigorating discussions, being good friends, and their herculean effort to keep me sane. I am grateful to my family, especially my parents, for being there for me all these years. I finished my education, and all of this would not have been possible without your continuous support.

Finally I want to thank Georg. I love you, you have been my rock, and without you I would be lost.

Annett Thogersen
April 2009

Preface

This study started in the autumn of 2004 and was funded by FUNMAT@UIO. The main work on this thesis was carried out at the Structure Physics research group at the Institute of Physics, University of Oslo. The PhD work was in cooperation with the Physical Electronics group at MINAlab, where another PhD student made the samples. My supervisors were Arne Olsen, Terje Finstad, and Bengt Svensson.

Part of my work was done during a four months research stay in the autumn of 2006 at the International Centre of Young Scientists (ICYS) at the National Institute of Material Science (NIMS) in Tsukuba, Japan. The results from my work there are present in all four papers. My supervisors at NIMS were Prof. Yoshio Bando and Dr. Masanori Mitome. The research stay was funded by a travel scholarship from FUNMAT@UIO, "Kristine Bonnevie" and SCANDEM.

My main work was to study Si, Ge, Er-oxide, and Pd nanocrystals and clusters in multilayer samples using different transmission electron microscopy and X-ray photoelectron spectroscopy techniques. Papers related to my Ph.D. work and collaborations with other groups that are not included in this thesis are presented below.

- J Mayandi, T G Finstad, S Foss, A Thøgersen, U Serincan and R Turan. Luminescence from silicon nanoparticles in SiO2: atomic force microscopy and transmission electron microscopy studies. *Physica Scripta* **T126**, 77 2006
- M. Avice, S. Diplas, A. Thøgersen, J. S. Christensen, U. Grossner, B. G. Svensson, O. Nilsen, H. Fjellvåg and J. F. Watts. Rearrangement of the oxide-semiconductor interface in annealed Al2O3/4H-SiC structures. *Applied Physics Letters* **91**, 052907 2007
- J. Mayandi, T.G. Finstad, S. Foss, A. Thøgersen, U. Serincan, R. Turan. Ion beam synthesized luminescent Si nanocrystals embedded in SiO2 films and the role of damage on nucleation during annealing. *Surface and Coatings Technology* **201**, 8482 2007
- J. Mayandi, T.G. Finstad, A. Thøgersen, S. Foss, U. Serincan, R. Turan. Scanning probe measurements on luminescent Si nanoclusters in SiO2 films. *Thin Solid Films* **515**, 6375 2007

- Spyros Diplas, Marc Avice, Annett Thogersen, Jens S. Christensen, Ulrike Grossner, Bengt G. Svensson, Ola Nilsen, Helmer Fjellvag, Steve Hinderc and John F.Watts. Interfacial studies of Al_2O_3 deposited on 4H-SiC(0001). *Surface and Interface Analysis* **40**, 822 2008

Table of Contents

Summary iii

Acknowledgments v

Preface vii

Contents ix

1 Introduction 1
References . . . 4

2 Nanostructured Memory Devices 5
2.1 Quantum dots . . . 5
2.2 Traditional flash memory devices . . . 8
2.3 Nanocrystal quantum dot memory storage devices . . . 9
2.4 Basic requirements for quantum dots in room temperature devices . . . 10
References . . . 11

3 Materials 13
3.1 Si nanocluster samples . . . 13
3.1.1 Silicon properties . . . 14
3.1.2 Defects . . . 17
3.2 Er-Si nanocluster samples . . . 18
3.2.1 Erbium properties . . . 19
3.3 Ge-Si-Pd nanocluster samples . . . 19
3.3.1 Germanium properties . . . 20
3.3.2 Palladium properties . . . 21
References . . . 22

4 Methodology 27
4.1 Transmission Electron Microscopy . . . 27
4.1.1 Transmission Electron Microscopes . . . 28
4.1.2 High Resolution Transmission Electron Microscopy . . . 28
4.1.3 Energy Dispersive Spectroscopy . . . 33

4.1.4 Electron Energy Loss Spectroscopy 35
4.1.5 Energy Filtered Transmission Electron Microscopy - Spectral Imaging . . 37
4.1.6 Scanning Transmission Electron Microscopy 38
4.2 X-ray Photoelectron Spectroscopy 39
4.2.1 Photoelectron escape depth 41
4.2.2 The binding energy 44
4.2.3 The chemical shift 45
4.2.4 Energy referencing, work function, and the chemical potential 47
4.2.5 Screening 50
4.2.6 Auger parameter 51
4.3 Secondary Ion Mass Spectrometry (SIMS) 53
References 54

5 Sample preparation **57**

6 Overview of papers **61**

Paper I:
A. Thogersen, J. Mayandi, T. Finstad,
J. S. Christensen, M. Mitome, Y. Bando and A. Olsen
Characterization of amorphous and crystalline silicon
nanoclusters in an ultrathin silica layer. **68**

Paper II:
A. Thogersen, S. Diplas J. Mayandi, T. Finstad,
M. Mitome, Y. Bando and A. Olsen
An experimental study of charge distribution in crystalline
and amorphous Si nanoclusters in thin silica films. **78**

Paper III:
A. Thogersen, J. Mayandi, T. Finstad,
S. Diplas, M. Mitome, Y. Bando and A. Olsen
The formation of Er-oxide nanoclusters in SiO_2
thin films with excess Si. **88**

Paper IV:
A. Thogersen, J. Mayandi, L. Vines, M. F. Sunding, T. Finstad,
S. Diplas, M. Mitome, Y. Bando and A. Olsen
Composition and electron beam assisted diffusion study of Pd- and Ge- containing nanoclusters in a SiO_2 matrix. **115**

List of Abbreviations **117**

List of Figures

2.1 A sketch of the energy bands and dielectric function of an atom, a bulk material and a nanocrystal quantum dot, adapted from Bimberg, Grundmann and Ledentsov [5] and Borovitskaya and Shur [6]. 6

2.2 A sketch of A) a regular flash memory device used today and B) a nanocrystal memory device. 9

3.1 A sketch of the different samples studied in this thesis. A) The Si samples studied in paper 1 and 2, B) the Er samples studied in paper 3, and C) the Ge-Pd-Si samples studied in paper 4. 15

3.2 A sketch of the indirect band gap in Si. 16

3.3 A sketch of two defects in an FCC type structure. A) A twin in the (110) plane with stacking ABCACBA, B) A stacking fault in between two twin boundaries. The figure is adapted from Verhoeven [3]. 17

4.1 The Contrast Transfer Function (CTF) of the JEOL 3100FEF. The top function is at Scherzer defocus (-37.0 nm), and the bottom function is at extended Scherzer defocus (-44.4 nm). 31

4.2 A plot of n/u^2 as a function of u^2. The plot was used for finding the focus of the HRTEM images in paper 1. The image in the bottom right corner shows a diffractogram of HRTEM image no. 10 and a diffraction pattern from the Si-substrate in the same sample. 33

4.3 The EDS process. 34

4.4 De-excitation mechanism for an atom that has undergone K-shell ionization and subsequently emission of a characteristic Kβ X-ray. 36

4.5 An EELS spectrum of Si showing the different peaks present, with an energy dispersion of about 0.8 eV. The inserted EELS image has a lower count on the y-axis (10^2). 37

4.6 The figure exhibits how an EFTEM-SI image is made up of an EELS spectrum in each point in the 2-dimensional image. The image at the top is made by the plasmon peak of Si, which lies at 16.8 eV. (Adapted from Ahn[11].) 38

4.7 The figure shows a sketch of Z-contrast/mass-thickness imaging. Thicker regions or regions with higher atomic number scatter more electrons off axes, causing them to show up as darker areas in the image. (Adapted from Williams and Carter [4].) 39
4.8 A survey spectrum of the sample investigated in paper 4, containing Si, SiO_2, Ge, and Pd. 40
4.9 The scattering process of a photon resulting in a photoelectron and an Auger electron. The figure is adapted from a book by Niemantsverdriet [13]. 41
4.10 The take-off angle ϕ and angle of emission θ. 43
4.11 A Wagner diagram plotted from the work in paper 1, of the samples with crystalline and amorphous Si nanoclusters. 53

5.1 A cross-sectional sample glued on a Cu slot. 58
5.2 Cu nanoclusters in SiO_2, introduced during surface preparation with too small grazing incidence angle of the sputter beam in the ion etcher. 59

Chapter 1

Introduction

Memory storage devices have been around since the 1960s, when Read Only Memories (ROM) were developed [1, 2, 3]. The ROMs could store up to hundreds or a few thousands bits of information, which is very small compared to today's technologies.

The first memory storage devices developed were Nonerasable Nonvolatile Memory Devices (NNMD). Nonvolatile means that no power is needed to maintain the information stored in the chip. These devices were built using small fuses, each of which represented one storage location, or 1 bit, where a blank ROM would have all fuses intact. Two types of NNMDs were developed, Programmable Read Only Memories (PROM) [4] and Mask Read Only Memories (MROM). PROM used the same concept as ROMs, but offered the convenience of programmable via a programmer, which means that the user had the ability to use a PROM programmer from his location and not have this task done for him. This device was still popular in the early 1970s.

Unfortunately the production of PROMs in mass quantities was time consuming and cumbersome. In the early 1980s MROMs were developed. The new MROMs used a code corresponding to the 0 or 1 pattern that needed to be programmed into the device. The manufacturer would then build a mask corresponding to this pattern and would use this mask to program a very large number of ROM. They could therefore achieve higher manufacturing efficiency and lower cost per device than was possible with pure ROM devices, and the MROMs were growing to quantities of millions of pieces per month in some applications. Their use continues in some applications today [2].

Erasable Nonvolatile Memory Devices as Erasable Programmable Read Only Memories (EPROM), One-Time Programmable Memories (OTP), and Electrically Erasable Programmable Read Only Memories (EEPROM) were discovered in the 1970s - 1980s. EPROM were discovered in 1971 by Dr Dov Frohman of Intel Corporation [1, 2, 3]. The basic storage element in an EPROM is a Metal-Oxide Semiconductor (MOS) transistor that has an additional floating gate built in between the control gate and the channel. The cell has a threshold voltage or a gate voltage at which the cell begins to conduct. When programming the device, an elevated voltage is applied to the gate and the drain of the cell. The electrons will then penetrate the oxide into the floating gate, thereby altering the threshold voltage of the cell by 5-10 V. The oxide is perfectly isolated by an insulator (ex. SiO_2), so that injected electrons cannot leak out of the floating gate after power is removed.

The production costs and time are significantly lower for EEPROMs than for standard PROMs. The EPROMs could erase an EPROM and reprogram it with the modified program, rather than having to incur the cost of a new PROM and wait the needed time for it to be programmed every time a new version of the software is written. The EPROMs became therefore the favoured memory device for product development and manufacture of end product with total production run of 10 000 units or less.

OTP gained popularity in the early-to-mid 1990s, to the point that they were used in millions of pieces per month in several applications. The OTP allows user to program them just once, but would be lower in cost than EPROMs, since they were housed in plastic packages as opposed to ceramic packages used for EPROMs. Today there are only a few companies that use the OTP memory device.

EEPROM devices could be erased and programmed in-circuit, as opposed to EPROMs that only could be programmed outside the circuit in which they are used. This could be done by exposing the cells to an electric charge. The device can only be erased a finite number of times because of the dielectric breakdown characteristics of the charge transfer oxides and the trapped charge in the oxides that eventually builds up to a level that causes improper operation. Earlier EEPROMs offered an endurance of only 100 program/erase cycles, while today's EEPROMs have improved this number to 10 000 program/erase cycles. Although newer technologies have replaced EEPROMs in many high-volume applications, EEPROMs still find use in some of today's applications.

Flash memory devices were developed in the early 1980s, when it became clear that the need for some upcoming applications surpassed the cumbersome byte-erase capability of the devices just discussed. The system performance could be much higher if the entire memory array or a large portion thereof could be erased quickly, so that new data could be written in its place.

Flash memory was implemented by Masuoka and Hisakazu [5, 6]. They worked at Toshiba Corporation and had already applied for a patent for simultaneously erasable EEPROMs in 1980. Two types of flash memory devices were developed, called NOR and NAND. The NOR and NAND gates are digital logic gates that implement logical NOR or NAND (truth-functional operator which produces a result that is the negation of logic) according to given tables. The new memory cell had only one cell which consisted of only one transistor. This costs far less than byte-programmable EEPROM and therefore has become the dominant technology wherever a significant amount of non-volatile, solid state storage is needed. The single-transistor cell has a simultaneous multibyte-erase scheme. Flash memory offers fast read access times and better kinetic shock resistance than hard discs. Also, when packaged in a memory card, it is extremely durable, being able to withstand intense pressure, extremes of temperature, and even immersion in water. The device has slow erase cycles, which means that the large block sizes used in flash memory erasing gives it speed advantage over the old style EEPROM when writing lots of data. Masuoka [5, 6] started working on a test chip in 1983, which led in 1985 to Toshiba's presentation, at the International Solid-State Circuits Conference (ISSCC), of a 256 kbit flash EEPROM device. This flash memory device uses a dual gate structure, in which the gate further from the silicon substrate is dubbed as the control gate, and the gate closer to the silicon substrate is dubbed the floating gate. Flash memory is mostly used in memory cards and USB (Universal Serial Bus) flash drives, for storage and transfer of data, and the use of this is discussed in the next chapter.

Silicon is widely used for electronic devices and is one of our most important semiconductor materials. It is used as floating gate in the memory devices, while SiO_2 is often used as the tunnel oxide, because of its good dielectric properties. One of the most important developments within the microelectronics industry is scaling the Si Complementary-Metal-Oxide-Semiconductor (CMOS) transistors down in size and generally improving the device further. The main challenges at nanoscale level are power and performance optimization, device fabrication, and control of variations at the nanoscale and integration of a diverse set of materials and devices on the same chip. A key element in one of the proposed schemes to meet future demands of downscaling is replacing the polycrystalline Si floating gate by nanocrystals. This can also

improve writing times, lower the gate voltage and lower the power consumption.

In this thesis, nanoclusters of Si, Ge, Er, and Pd were embedded in an SiO_2 film, in order to study their composition, nucleation, distribution, and atomic and electronic structure with different heat treatments and compositions. This was done using High Resolution Transmission Electron Microscopy (HRTEM), Energy Filtered TEM (EFTEM), X-ray Photoelectron Spectroscopy (XPS), Electron Energy Loss Spectroscopy (EELS), Secondary Ion mass Spectroscopy (SIMS), and Energy Dispersive X-ray Spectroscopy (EDS).

References

[1] P. CAPPELLETTI, C. GOLLA, P. OLIVO, and E. ZANONI, *Flash Memories*, Springer, 1999.

[2] V. G. OKLOBZIJA, *Digital Design and Fabrication*, CRC Press, 2007.

[3] F. E. VALDES-PEREZ, V.-P. F. E. STAFF, and R. PALLAS-ARENY, *Microcontrollers: Fundamentals and Applications with PIC*, CRC Press, 2009.

[4] US-Switch Matrix- Patent 3028659.

[5] WWW.FORBES.COM, 2009.

[6] F. MASUOKA and I. HISAKAZU, US patent 4531203.

Chapter 2

Nanostructured Memory Devices

Nanostructured memory devices are suggested to be an improvement to the flash memory devices used today. Nanocrystals have the potential to be used in different applications, such as optical amplifiers, photon converters, and memory storage devices [1, 2, 3, 4] to mention just a few. Nanocrystal memory cells have potentially better electronic performance than current technology offers, and those properties in combination with features inherent in the concept is considered to yield a possibility for scaling the devices considerable down in size which is desired from economic and technological reasons. An interesting property of semiconductor nanocrystals is its ability to store charge over time at room temperature when embedded in an oxide layer.

This chapter contains a short introduction to quantum dots and flash memory devices. In addition, expected improvements from the usage of nanocrystals instead of the normal bulk floating gate are given.

2.1 Quantum dots

In any semiconductor material, electrons can only attain certain energy levels. In a bulk semiconductor, the energy levels are so close together with only small differences in energy, that, for practical purposes, they form a continuous spectrum. Some energy intervals have no states available for electrons, and such gaps in energy form the energy band gap, see Figure 2.1. Different

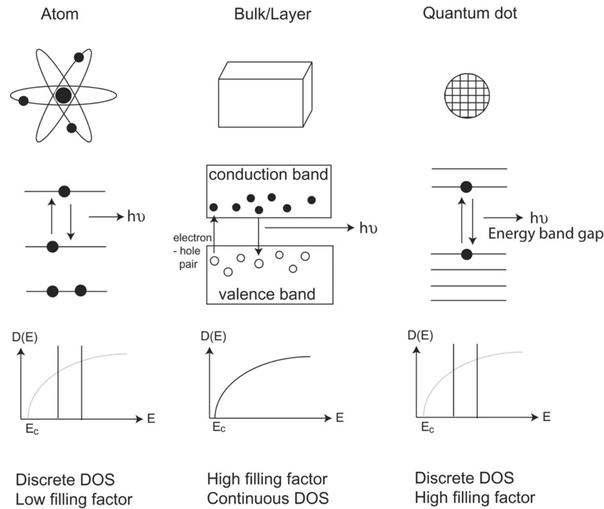

Figure 2.1: *A sketch of the energy bands and dielectric function of an atom, a bulk material and a nanocrystal quantum dot, adapted from Bimberg, Grundmann and Ledentsov [5] and Borovitskaya and Shur [6].*

semiconductor materials have different band gaps, and quantum dot nanocrystals, being made from semiconductor materials, are therefore characterized by their band gaps.

In what follows, the different regimes for the so called confinement will be discussed with regards to the size of the confinement.

If the size of the nanocrystals is of the same order as the exciton Bohr radius and the de Broglie wave length, the energy levels cannot be described as continuous. Instead, they occupy discrete energy levels (quantum confinement), and size quantization effects can be observed [7, 5]. This means that quantum dots have large level spacing with a defined boundary between the matrix and the quantum dot. Because of their discrete energy levels, the quantum dots are more related to an atom than to a bulk material, see Figure 2.1.

The exciton Bohr radius is the distance between an excited electron and the corresponding hole (electron-hole pair), see Figure 2.1. The exciton Bohr radius and an evaluation of the quantum confinement with varying quantum dot radius is presented. The radius can be calculated from the sub-band energy separation ($E_{sub-band}$) and the exciton binding energy ($E_B^{exciton}$) [8]. The

sub-band energy separation ($E_{sub-band}$) of the electron or the corresponding hole is given by [8]

$$E_{sub-band} = \frac{\hbar^2 D}{2m_{e(h)}R^2} \quad (2.1)$$

where R is the quantum dot radius, $m_{e(h)}$ is the effective mass of the electron (hole) and D is a numerical factor. This factor depends on the shape of the quantum dot and is typically about 10 for a spherical quantum dot. The exciton binding energy ($E_B^{exciton}$) in the bulk is given by [8]

$$E_B^{exciton} = \frac{\hbar^2}{2\mu(a_B^*)^2} \quad (2.2)$$

where μ is the electron-hole reduced mass and a_B^* is the exciton Bohr radius. When assuming $m_e \ll m_h$, the criterion for higher hole sub-bands to be included is given by $E_{sub-band} \leq E_B^{exciton}$ [8]. That is

$$\frac{D}{m_h R^2} \leq \frac{1}{m_e(a_B^*)^2} \quad (2.3)$$

which can be rewritten to

$$\left(\frac{R}{a_B^*}\right)^2 \geq \frac{m_e}{m_h} D \quad (2.4)$$

At strong quantum confinement the quantum dot radius is much smaller than the exciton Bohr radius, i.e. $R/a_B^* \ll 1$. At that point the $E_B^{exciton}$ is of the order of $E_{sub-band}$ and much lower than the electron-hole Coulomb interaction, and the exciton ground state is mainly composed of the lowest-energy sub-band states. As the quantum dot radius increases, the energy separation of the sub-bands becomes comparable with $E_B^{exciton}$, and it can even get smaller. In this region there is intermediate confinement, and higher sub-band states are even mixed into the exciton ground state. Increasing the quantum dot radius further results in weak quantum confinement. Here the quantum dot radius is much larger than $E_B^{exciton}$, and the sub-bands are distributed almost continuously. The electron-hole binding energy is nearly the same as in the bulk material [8].

The de Broglie wave length (λ) can be expressed as [6]

$$\lambda = \frac{h}{p} = \frac{6.22}{\sqrt{\frac{m_{\text{eff}}}{m_0}\frac{T}{300}}} \tag{2.5}$$

where p the particle momentum, h is Planck's constant, m_{eff} is the effective electron mass, m_0 is the electron mass, and T the temperature. The de Broglie wave length varies from a fraction of one nanometer to 10-20 nm.

Because the energy levels of the quantum dot are discrete rather than continuous, adding or extracting only one electron can change the properties of the quantum dot dramatically, like altering the boundaries of the band gap. Variations in the geometry of the quantum dot can also alter the band gap. Because of the small size of the quantum dot, the band gap will always be larger than for the same semiconductor bulk material.

2.2 Traditional flash memory devices

A flash memory device is used as non-volatile computer memory, which means that no power is needed to keep the stored information in the computer chip. A sketch of a typical flash memory device is presented in Figure 2.2A. Charge can be stored by tunnelling electrons into the floating gate (usually Si) through the tunnel-oxide (usually SiO_2) by applying the proper voltage (V_g) over the tunnel-oxide. The charge can be stored over time within the floating gate at room temperature.

The high dielectric constant of the oxide prevents electrons from tunnelling out of the floating gate. If a material with a high dielectric constant is placed in an electric field, the magnitude of that field will be reduced within the volume of the dielectric. In this manner, the dielectric constant of the oxide together with the excited levels of the quantum dot (floating gate), keeps the electrons from tunnelling out, preventing memory loss. Although one would prefer the oxide to be as thin as possible in order to minimize the size of the device, it needs to be thick enough to keep the electrons from tunnelling out of the floating gate. The memory can be read by checking if the Metal-Oxide-Semiconductor (MOS) transistor is on or off. If the MOS transistor is on, a

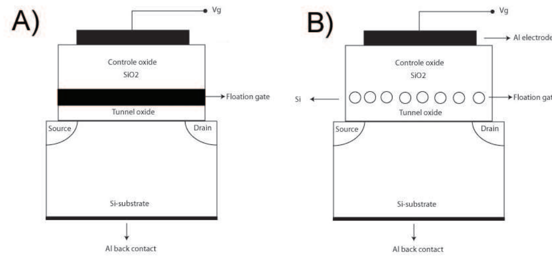

Figure 2.2: *A sketch of A) a regular flash memory device used today and B) a nanocrystal memory device.*

current is flowing between the source and the drain. The nanocrystals can be filled or drained accordingly.

Flash memory devices are mainly used in memory cards and USB flash drives in laptops, digital cameras, Personal Digital Assistant's (PDA), mobile phones, etc. When a flash memory device is part of a memory card, it can withstand extreme temperatures and pressures, and it can even be immersed in water.

Using the wide floating gate of traditional flash memories, there is a limit to how small the device can be, the amount of memory that can be stored, and a limit to the storing time. As for now, new types of memory cards (RS-MMC, miniSD, microSD and Intelligent Stick) that have been developed have form factors with an area of 1.5 cm^2 and a thickness of less than 1 mm. Their memory capabilities range from 64 MB to 16 GB (October 2008) [9]. By replacing the bulk floating gate with nanocrystals, these properties might improve.

2.3 Nanocrystal quantum dot memory storage devices

When tunneling the electrons through the SiO_2 layer and into the silicon, the charge can be stored within the nanocrystals. The electrical charge carriers in the semiconductor nanocrystal have electric field lines passing through the surrounding medium with a smaller dielectric constant than in the nanocrystal. Because of this, the screening effect is reduced, and the Coulomb interaction between charge carriers is enhanced. This increases $E_B^{exciton}$ and the exciton oscillator

strength compared to the situation with a surrounding matrix with the same dielectric constant as Si or by pure Si [8]. Between the nanocrystal and the matrix, there is a potential barrier acting such that the electrons are trapped within the nanocrystal. As the quantum dots are small, adding or removing only one electron will alter the material properties on a large scale. Because of this, the properties of the nanocrystals are somewhere between those of bulk semiconductors and those of discrete molecules.

By replacing the bulk floating gate with nanocrystals, longer retention may result in lower gate voltage and lower power consumption [10]. The non-continuity between the nanocrystals can also prevent charge loss laterally and result in short writing times at lower voltages and improved reliability [11]. Nanocrystals with a diameter of less than 10 nm are desirable, since the Coulomb blockade effect becomes prominent at room temperature [12]. When the dimensions approach the atomic scale, nanocrystals start to differ significantly from bulk materials in their electronic, optical and thermodynamic properties [13]. In these nanocrystal memory devices, the processes of injection and retention of electrons are very sensitive to the size, distribution, interfaces and electronic structure of the nanocrystals. It is therefore important to study the nucleation mechanisms of the nanocrystals, their crystal structure, defects, and distribution, in order to make devices in a controlled manner. The devices need an accurate control of the array of nanocrystals, since changing the tunnel distance by only one nanometer can affect the write and erase time [14].

2.4 Basic requirements for quantum dots in room temperature devices

Some of the basic requirements for quantum dots operating at room temperature are discussed below. As discussed above, the quantum dots should be small. There is, however, a lower size limit. This critical diameter size D_{min} occurs where at least one energy level of an electron or hole is present [5]. This lower size limit depends strongly on the band offset of the corresponding bands in the material system. One electron level exists only if the confinement potential exceeds the value D_{min}, which is defined by [5]

$$D_{min} = \frac{\pi\hbar}{\sqrt{2m_e^*\Delta E_c}} \tag{2.6}$$

where m_e^* is the effective electron mass and ΔE_c is the conduction band offset.

A certain level of uniformity in size, shape, and chemical composition are needed to get a stable device. In addition, the nanocrystal quantum dots should be free of defects like dislocations and twins. The size fluctuations cause a variation in the energy position of the electronic levels. Quantum dots rely on the integrated gain in narrow energy range, which means that the inhomogeneous energetic broadening should be as small as possible [5].

References

[1] S. TIWARI, F. RANA, H. HANAFI, A. HARTSTEIN, E. F. CRABBE, and K. CHAN, *Appl. Phys. Lett.* **68**, 1377 (1996).

[2] H. S. HAN, S. Y. SEO, and J. H. SHIN, *Appl. Phys. Lett.* **79**, 4568 (2002).

[3] P. KIK and A. POLMAN, *J. Appl. Phys.* **91**, 534 (2002).

[4] L. PAVESI and D. J. LOCKWOOD, *Silicon Photonics*, Springer-Verlag, 2004.

[5] D. BIMBERG, M. GRUNDMANN, and N. LEDENTSOV, *Quantum Dot heterostructures*, Wiley, 1999.

[6] E. BOROVITISKAYA and M.S.SHUR, *Quantum dots, Low dimensional systems*, chapter 1, p. 1, World Scientific, 2002.

[7] WWW.EVIDENTTECH.COM, 2008.

[8] Y. MASUMOTO and T. TAKAGAHARA, *Semiconductor Quantum Dots: Physics, Spectroscopy, and Applications*, Springer, 2002.

[9] http://www.sandisk.com/Corporate/PressRoom/PressReleases/PressRelease.aspx?ID=4398, 2008.

[10] T. P. CHEN, Y. LIU, C. Q. SUN, M. S. TSE, J. H. HSIEH, Q. Y. FU, Y. C. LIU, , and S. FUNG, *J. Phys. Chem. B* **108**, 16609 (2004).

[11] F. KARADAS, G. ERTAS, and S. SUZER, *J. Phys. Chem. B* **108**, 1515 (2004).

[12] S. NAITO, M. SATAKE, H. KONDO, M. SAKASHITA, A. SAKAI, S. ZAIMA, and Y. YASUDA, *Jpn. J. Appl. Phys.* **43**, 3779 (2004).

[13] T. MOHANTY, N. C. MISHRA, A. PRADHAN, and D. KANJILAL, *Surf. Coat. Technol.* **197**, 34 (2005).

[14] M. PEREGO, S. FERRARI, M. FANCIULLI, G. B. ASSAYAG, C. BONAFOS, and A. C. M. CARRADA, *Appl. Surf. Sci.* **231-232**, 813 (2004).

Chapter 3

Materials

In this chapter, a brief introduction to the different material systems studied in this work is presented. In the papers presented in this work, samples containing Si, Ge, Er, and Pd nanoclusters were studied in detail. In the following sections the samples and their sample processing conditions are discussed in detail.

3.1 Si nanocluster samples

In papers 1 and 2, amorphous and crystalline nanoclusters of Si were studied. These samples were made by growing a $\sim$3 nm thin layer of SiO_2 on a p-type silicon substrate by Rapid Thermal Oxidation (RTO) at $1000°$C for 6 seconds. By precise control of the oxidation temperature and reducing the thermal budget of the heat cycle required for an oxide film growth, the effects of oxidation on the impurity profile can be controlled and minimized.

Prior to growing the RTO layer, the wafers were cleaned using a standard RCA procedure (Radio Corporation of America, industry standard for removing contaminants from wafers [1]) followed by immersion in a 10 % HF solution to remove the native oxide. Then a $\sim$10 nm layer of silicon rich oxide was sputtered from a SiO_2:Si composite target onto the RTO and heat-treated in a N_2 atmosphere at $1000 - 1100°$C for 30-60 minutes. Different area percentages (defined below) of Si:SiO_2 (6, 8, 17, 28, 42, 50, 60, 70 area % or about 4, 5, 11, 18, 33, 40, 46 atomic %) were

used to produce different silicon super saturation in the oxide. A sketch of this type of samples is presented in Figure 3.1A for the cases where Si nanoclusters have formed in the oxide.

The atomic percentage of the different elements in the sample can be calculated from the area percentages. The equation for the atomic percentage of excess Si in SiO_2 is

$$\text{atomic\%} = \frac{\text{area\%}(\text{Si}_{\text{Si}}) \cdot \text{spc}(\text{Si}_{\text{Si}})}{\text{area\%}(\text{Si}_{\text{Si}}) \cdot \text{spc}(\text{Si}_{\text{Si}}) + \text{area\%}(\text{SiO}_2) \cdot (\text{spc}(\text{Si}_{\text{SiO}_2}) + \text{spc}(\text{O}_{\text{SiO}_2}))} \quad (3.1)$$

where the sputtering coefficients (spc) are 0.7622 for Si in pure Si, 1.88 for Ge in pure Ge, 2.42 for Er in pure Er, 0.295 for Si and 0.622 for O in SiO_2.

3.1.1 Silicon properties

In 1787, silicon was first identified by Antoine Lavoisier as one of the components of *silex* or *silicis*, which means flint or hard rock, and is now called *silica* or *silicates*. It wasn't until 1823 that Si was isolated as an element by J.J. Berzelius, a Swedish chemist.

Silicon is present in the sun and other stars and is a principal component of a class of meteorites known as aerolites [2]. Si makes up 25.7% of the earth crust. It is the second most abundant element, exceeded only by oxygen [2], and has so far been the most important semiconductor.

Pure Si is rarely found in nature. The most common places to find Si is in silica or silicates (various minerals containing Si, O, and one or several other metals), but can also be found in quartz, rock crystal, amethyst, agate, flint, jasper, opal, asbestos, feldspar, clay, and mica [2]. Crystalline silicon has a grey colour and a metallic lustre. It has characteristics similar to glass, as it is very brittle and prone to chipping. Crystalline Si has a cubic diamond type structure with a cell dimension $a = 0.543$ nm, and its electron configuration is $[\text{Ne}]3s^2 3p^2$.

Si has good mechanical properties, and there is an increasingly growing research field around this material. Pure Si is an important component in semiconductor devices, especially in integrated circuits. Si is a desirable material because it remains a semiconductor even at higher temperatures, and its native oxide is easily grown in a furnace and forms a better semiconduc-

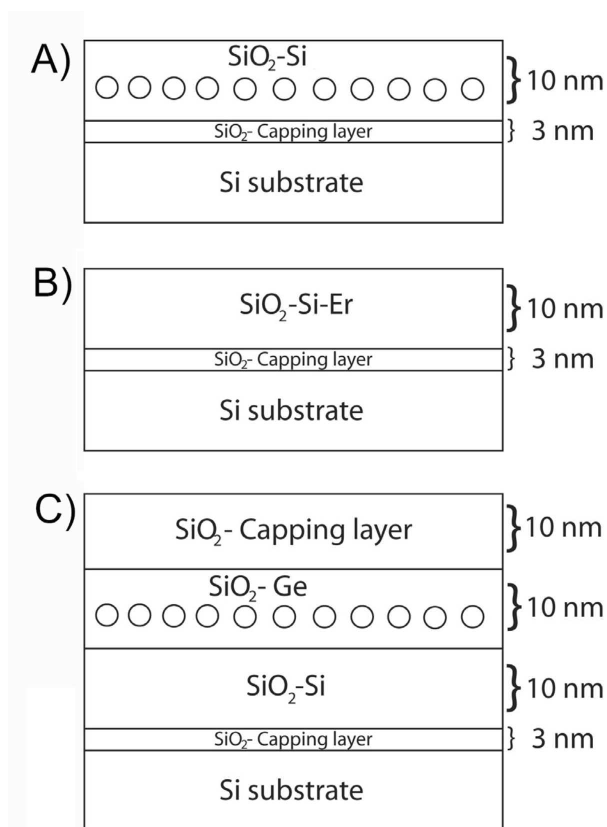

Figure 3.1: *A sketch of the different samples studied in this thesis. A) The Si samples studied in paper 1 and 2, B) the Er samples studied in paper 3, and C) the Ge-Pd-Si samples studied in paper 4.*

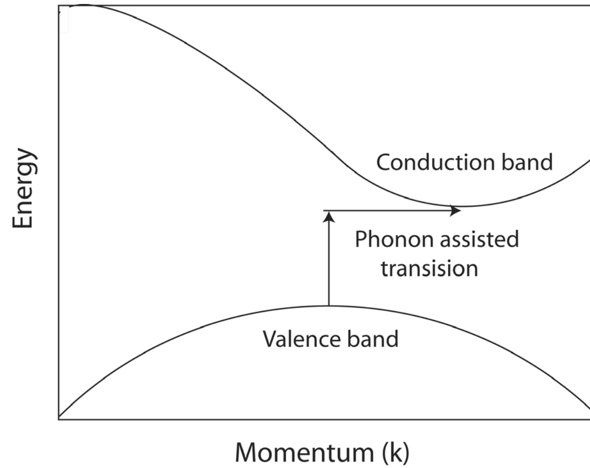

Figure 3.2: *A sketch of the indirect band gap in Si.*

tor/dielectric interface than any other material. The raw materials are relatively cheap, and the integrated opto-electronic silicon can be used in telecommunication, information technology, and microtechnology.

As depicted in Figure 3.2, Si has an indirect band gap, which is the energy gap in which the minimum energy in the conduction band is shifted by a k-vector (difference in momentum) relative to the valence band.

When electrons are excited to the conduction band, the electrons quickly settle into the energy minimum. For the electrons to fall back into the valence band, the electrons require extra momentum allowing them to overcome the offset. Emitted and absorbed photons have high energy, but negligible momentum compared to this energy offset. Because of this, indirect semiconductor materials are inefficient for emitting light, which involves electron-hole recombination. Electron-hole recombination can therefore take some time and take place preferentially at point defects, dislocations or at grain boundaries.

The absorption of light at an indirect band gap is weaker than at a direct band gap. The only way for an electron to jump from the valence band maximum to the conduction band minimum is to simultaneously emit or absorb a phonon. This would then compensate for the missing momentum (k-vector), but this transition has a very low probability.

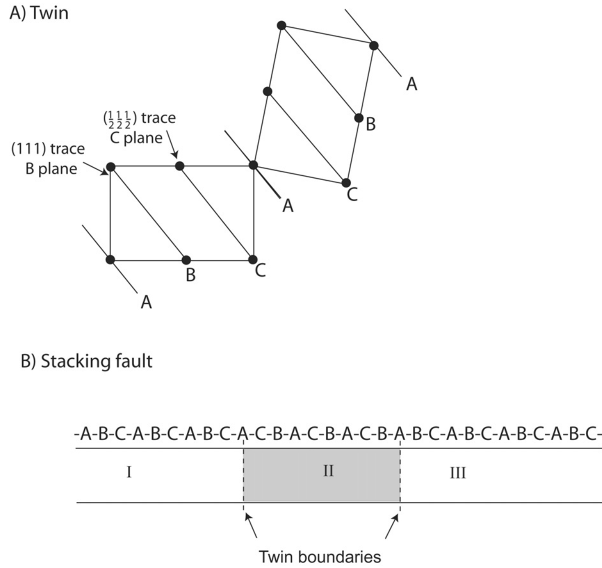

Figure 3.3: A sketch of two defects in an FCC type structure. A) A twin in the (110) plane with stacking ABCACBA, B) A stacking fault in between two twin boundaries. The figure is adapted from Verhoeven [3].

3.1.2 Defects

Silicon has a diamond type FCC crystal structure, where some of the most common defects are point defects, dislocations, twinning, and stacking faults. In paper 1, nanocrystals containing twins and stacking faults were found. These defects and their effects upon the memory device are discussed below.

Twinning is a change in stacking sequence over many atomic layers that results in two crystalline grains sharing some of the same crystalline positions at the interface [3]. This interface with shared atomic sites separating the two crystals is called the twin boundary. A sketch of a twin in an FCC crystal structure is shown in Figure 3.3A. The twinned stacking sequence shown in the Figure is ABC **A** CBA, where the twin boundary is at the A position in the middle. The twinning results in a mirror image of the other crystal grain.

Twinning can be formed in a crystal in different manners, like during deformation or crystal

growth [3]. A Growth twin can be formed as a result of changes in the stacking during growth. They can be formed in a crystal whether it is growing from vapor, liquid, or solid state. Another twin formation is called Annealing or Transformation twin. This can occur as a result of changes in the crystal systems during cooling. One form becomes unstable and the crystal structure must re-organize or transform into another more stable form. It is common for FCC type metals to form growth twins during relaxation. A third twin formation is called Deformation or Glide twin. This twin formation is a result of stress on the crystal after the crystal has formed. During deformation of metals, slip is generally more easily generated than twinning. Twinning will only be a significant mechanism for plastic deformation in non-cubic metals (ex. Hexagonal Closed Packed (HCP) metals). This type of metals has only a few slip systems available. Deformation twinning in FCC type metals are rare and may only occur at very low temperatures [3].

Stacking faults are two dimensional defects that can be seen as a change in stacking sequence over a few atom spacings, see Figure 3.3B. In the figure, twin orientation I and III have identical crystallographic orientations. Region II is separated from region I and III by two twin boundaries. If this region is separated by a few nanometers, it will be called a twin. If it is separated by only a few atomic spacings, it will be called a stacking fault [3]. The stacking fault is in a sense two twin boundaries and can be made up by only one atomic plane, as in ABCAB **A** BCABC.

Twinning depends on the stacking fault energy of the material, the crystallographic orientation, surface stresses, and surface orientations [4, 5]. Defects and imperfections either inside the nanocrystal or at the nanocrystal/oxide interface can have large effects upon the operational characteristics of the device [5, 6, 7, 8]. Nanocrystal twinning can be due to stress inside the nanocrystal and on the surface, coalescence of smaller nanocrystals, or it can occur during growth/heat-treatment.

3.2 Er-Si nanocluster samples

In paper 3, SiO_2 with both Er and Si were made by growing a $\sim$3 nm layer of SiO_2 on a p-type Si substrate by Rapid Thermal Oxidation (RTO) at 1000^oC for 6 sec. Then a layer of Er-doped Si rich oxide was sputtered from a SiO_2:Si:Er composite target onto the RTO with a 30 nm oxide thickness. The percentages of Si and Er are 17 area % (11 at. %) and 1.1 area % (1 at. %) respectively. The samples were then heat treated in a N_2 atmosphere at $1000 - 1100^o$C for 30-60

min. A sketch of the samples discussed in this paper is presented in Figure 3.1B.

3.2.1 Erbium properties

The name Erbium (Er) originates from a town in Sweden called Ytterby where large concentrations of Yttria and Erbium were found. The material was discovered in 1843 by Carl Gustaf Mosander. In 1905 Georges Urbain and Charles James isolated ErO_2, but pure Er wasn't produced until 1934, when workers reduced the anhydrous chloride with potassium vapour.

Er is a silvery, white, metallic, rare earth element. Pure Er is easily shaped, does not oxidize as easily as other rear earth elements, and is stable in air. Erbium's properties partly depend on the amount and type of impurities present in the material. This element cannot be found as a pure element in nature, but is found bound in monazite and sand ores.

The (indirect) excitations of Er atoms from Si nanocrystals are useful for optical applications, like light-emitting diodes and lasers [9, 10]. Si was for a long time considered unsuitable for optoelectronic applications due to silicon's indirect band gap and the absence of linear electro-optic effect. However, doping of Er into the Si structure has avoided this problem [11]. The Er electronic configuration of Er is $[Xe]=4f^{12}6s^2$, with an electron shell structure of: 2,8,18,30,8,2 [2]. This shows that Er has an unfilled 4f shell surrounded by an external closed shell [11]. Intra 4f-transitions ($4l_{13/2}$ to $4l_{15/2}$) will therefore show luminescence at 1.54 μm, which is concordant with the absorption minimum in silicon-based glass fibers [10, 12]. This transition can be excited both optically [13] and electrically [14]. The sensitizing of Er by Si nanocrystals have been studied by many authors and is currently an active field of research [15, 16, 17, 18, 19, 20].

3.3 Ge-Si-Pd nanocluster samples

In paper 4, Ge and Pd nanoclusters in the presence of pure Si were studied. The samples were produced by growing a $\sim$3 nm layer of SiO_2 on a p-type silicon substrate by Rapid Thermal Oxidation (RTO) at 1000°C for 6 sec. Prior to growing the RTO layer the wafers were cleaned using a standard RCA procedure (Radio Corporation of America, industry standard for removing contaminants from wafers) followed by immersion in a 10 % HF solution to remove the native

oxide. After the RTO growth a $\sim$10 nm layer of silicon rich oxide was sputtered from a SiO_2:Si composite target onto the RTO-SiO_2 and heat treated in N_2 atmosphere at 1000°C for 30 min. Different area percentages (area coverage by the sputtered material) of Si:SiO_2 (28, 42, 50, 60, 70% or 4, 5, 11, 33, 40, 46 at. %) were achieved. A $\sim$10-13 nm Ge rich (3.3 area %) SiO_2 with a 10 nm SiO_2 capping layer was then sputtered onto the Si rich oxide, with a subsequent heat-treatment at 900°C for 30 min to nucleate Ge nanocrystals. A sketch of the material systems discussed in this paper is presented in Figure 3.1C. During this last procedure, contamination of Pd occurred. This contamination resulted in a creation of Pd nanocrystals in the sample. These nanoclusters were studied in detail.

3.3.1 Germanium properties

Ge was predicted by Dmitri Mendeleev in 1871 to exist as a missing analogue of the silicon group [21]. Ge was first proven to exist in 1886, by Clemens Winkler, a German chemist [22]. The Ge transistor was developed in 1948 [23]. This discovery resulted in a demand for using Ge in solid state electronics devices [24]. Ge has favourable properties utilized in several optic and electronic devices, such as photo detectors and single transistors [25, 26]. Potential future applications may also exploit these for example in photo detectors [27], light emitters [28], single electron transistors [29], and non-volatile memories [30].

Ge is a hard, lustrous, greyish-white metalloid. In its pure state it is crystalline, brittle and retains its lustre in air at room temperature. Ge has an indirect band gap and has an FCC crystal structure (Fm-3m) with a cell dimension $a = 0.566$ nm, and the electronic configuration is [Ar]$3d^{10}4s^24p^2$ [2].

Substantial research has previously been devoted to characterizing Ge nanocrystal nucleation, diffusion, and growth [31, 32, 33, 34, 35, 36, 37, 38, 39]. Ge implantation in SiO_2 layers has so far been extensively studied for their photoluminescence and structural properties. Ge is also of interest because of its smaller bandgap, inducing a theoretically better retention and faster writing/erasing times [40, 41].

3.3.2 Palladium properties

Pd is a silvery white metal that was discovered in 1803 by William Hyde Wollaston [42, 43]. He named the metal Pallas after the asteroid which was discovered two years earlier.

Palladium, platinum, rhodium, ruthenium, iridium, and osmium form a group of elements called "platinum group metals" (PGMs). These metals share similar chemical properties. Pd has the lowest melting point and is the densest of these metals. During annealing Pd gets soft and ductile. At room temperature Pd can absorb 900 times its own volume of hydrogen, which makes Pd an efficient and safe storage medium for hydrogen isotopes.

Pd is mostly used for catalytic converters in auto mobiles [44], but can also be found in electronic devices such as computers, mobile phones, multi-layer ceramic capacitors, component plating, low voltage electrical contacts, and televisions [45]. The metal can also be used in dentistry [46], hydrogen purification, chemical applications, medicine, groundwater treatment, and fuel cells. Considerable research has also been conducted in the use of Pd catalysts for the combustion of methane. Particle morphology and oxidation state can play an important role in defining the active sites in the Pd catalysts [47]. Pd is also an interesting material used in Granular Metal (GM) films, cermets, or nano-cermets, where metal particles are dispersed in an insulator [48, 49]. The lower dimensional mesoscopic materials with tunnelling junctions have a negative coefficient of resistance, where the resistance increases with decreasing temperature.

Pure Pd has a Fm-3m space group, with a lattice parameter of 0.389 nm [50]. The electron per shell configuration for Pd is [2]: 2,8,18,18,0. This shows that Pd has an outer closed shell. Pd is a fast interstitial diffuser and almost insoluble in crystalline Si. The solubility of fast diffusing species in amorphous Si is known to be higher than that in crystalline Si and very sensitive to the defect concentration [51]. Pd does not dissolve Ge, and the solubility of Pd in Ge has not been studied [52]. Pd in SiO_2 has been studied by Ichinohe et al. [48, 49], who studied Pd doped SiO_2 films and found at small doses of Pd ultra fine particles of Pd_2Si. Voogt et al. [53] studied PdO particles with a metallic Pd core.

References

[1] http://fabweb.ece.uiuc.edu/recipe/rca.aspx, 2009.

[2] WEBELEMENTS.COM, The periodic table, 2008.

[3] J. D. VERHOEVEN, *Fundamentals of Physical Metallurgy*, Wiley, 1975.

[4] H. S. PARK, K. GALL, and J. A. ZIMMERMAN, *J. Mech. Phys. Solids* **54**, 1862 (2006).

[5] Y. Q. WANG, R. SMIRANI, and G. G. ROSS, *Nano Lett.* **4**, 2041 (2004).

[6] C. Q. SUN, L. K. PAN, Y. Q. FU, B. K. TAY, and S. LI, *J. Phys. Chem. B Lett.* **107**, 5113 (2003).

[7] Y. Q. WANG and R. S. NAD G. G. ROSS, *Appl. Phys. Lett.* **86**, 221920 (2005).

[8] C. R. PERRY, S. THOMPSON, M. LENTZEN, U. KORTSHAGEN, and C. B. CARTER, *J. Non-Cryst. Solids* **343**, 78 (2004).

[9] MELDRUM, A. HRYCIW, A. MACDONALD, C. BLOIS, T. CLEMENT, R. DECORBY, J. WANG, and Q. LI, *J. Lumin.* **121**, 199 (2006).

[10] H. ENNEN, J. SCHNEIDER, G. POMRENKE, and A. AXMANN, *Appl. Phys. Lett.* **43**, 943 (1983).

[11] C. ZHANG, H. XIAO, Y. WANG, Z. CHENG, X. CHENG, and F. ZHANG, *Physica B* **362**, 208 (2005).

[12] M. FUJII, M. YOSHIDA, Y. KANZAWA, S. HAYASHI, and K. YAMAMOTO, *Appl.Phys. Lett.* **71**, 1198 (1997).

[13] G. FRANZO, F. PRIOLO, S. COFFA, A. POLMAN, and A. CARNERA, *Appl. Phys. Lett.* **64**, 2235 (1991).

[14] J. MICHEL, J. BENTON, R. FERRANTE, D. JACOBSON, D. EAGLESHAM, E. FITZGERALD, Y.H.XIE, J. POATE, and L. KIMERLING, *J. of Appl. Phys.* **70**, 2672 (1991).

[15] C. CHRYSSOU, D. PACIFICI, V. VINCIGUERRA, F. PRIOLO, and F. IACONA, *Appl. Phys. Lett.* **75**, 2011 (1975).

[16] J. H. Shin, M. Kim, S. See, and C. Lee, *Appl. Phys. Lett.* **72**, 1092 (1998).

[17] P. Kik and A. Polman, *J. Appl. Phys.* **91**, 534 (2002).

[18] A. Kenyon, C. Chryssou, C. Pitt, T. Shimizu-Iwayama, D. Hole, N. Sharma, and C. Humphreys, *J. of Appl. Phys.* **91**, 367 (2002).

[19] F. Xu, Z. Xiao, G. Cheng, Z. Yi, T. Zhang, L. Gu, and X. Wang, *Thin Solid Films* **410**, 94 (2002).

[20] D. M. Zhigunov, O. Shalygina, S. Teterunkov, V. Y. Timoshenko, P. Kashkarov, and M. Zacharias, *Semicond. Sci. Technol.* **40**, 1193 (2006).

[21] M. Kaji, *Bull. Hist. Chem.* **27**, 4 (2002).

[22] C. Winkler, *Ber. Dtsch. Chem. Ges.* **19**, 210 (1887).

[23] J. Bardeen, *Phys. Rev. B* **74**, 230 (1948).

[24] National Academy of Engineering (http://www.greatachievements.org/?id=3967), 2008.

[25] S. Agan, A. Dana, and A. Aydinli, *J. Phys.: Condens. Matter* **18**, 5037 (2006).

[26] R. Salh, L. Fitting, E. V. Kolesnikova, A. A. Sitnikova, M. V. Zamoryan-skaya, B. Schmidt, and H.-J. Fitting, *Semiconductors* **41**, 387 (2007).

[27] K. L. Wang, J. L. Liu, and G. Jin, *J. Cryst. Growth* **237-239**, 1892 (2002).

[28] Y. Q. Wang, G. L. Kong, W. D. Chen, H. W. Diao, C. Y. Chen, S. B. Zhang, and X. B. Liao, *Appl. Phys. Lett.* **81**, 4174 (2002).

[29] D. V. Averin and K. K. Likharev, *J. Low-Temp. Phys.* **77**, 2394 (1986).

[30] M. Kanoun, , A. S. A. Baron, and F. Mazen, *Appl Phys. Lett.* **84**, 5079 (2004).

[31] Y. Maeda, *Phys. Rev. B* **51**, 1658 (1995).

[32] J. von Borany, R. Grötzschel, K. H. Heinig, A. Markwitz, B. Schmidt, W. Skorupa, and H. J. Thees, *Solid State Electronics* **43**, 1159 (1999).

[33] W. K. Choi, Y. W. Ho, S. P. Ng, and V. Ng, *J. Appl. Phys.* **89**, 2168 (2001).

[34] W. K. Choi, W. K. Chim, C. L. Heng, L. W. Teo, V. Ho, V. Ng, D. A. Antoniadis, and E. A. Fitzgerald, *Appl. Phys. Lett.* **80**, 2014 (2002).

[35] M. Klimenkov, J. von Borany, W. matz, R. Grötzschel, and F. Hermann, *J. Appl. Phys.* **91**, 10062 (2002).

[36] G. Taraschi, S. Saini, W. W. Fan, and L. Kimerling, *J. of Appl. Phys.* **93**, 9988 (2003).

[37] E. S. Marstein, A. E. Gunnæs, A. Olsen, T. G. Finstad, R. Turan, and U. Serincan, *J. Appl. Phys.* **96**, 4308 (2004).

[38] W. K. Choi, V. Ho, V. Ng, Y. W. Ho, S. P. Ng, and W. K. Chim, *Appl. Phys. Lett.* **86**, 143114 (2005).

[39] V. Beyer and J. von Borany, *Phys. Rev. B* **77**, 014107 (2008).

[40] S. Duguaya, A. Slaoui, J. Grob, M. Kanoun, S. Burignat, and A. Souifi, *Mater. Sci. and Engeneer. B* **124-125**, 488 (2005).

[41] M. Kanoun, A. Souifi, T. Baron, and F. Mazen, *Appl. Phys. Lett.* **84**, 5079 (2004).

[42] W. P. Griffith, *Platinum Met. Rev.* **47**, 175 (2003).

[43] W. H. Wollaston, *Philos. Trans. R. Soc. London* **94**, 419 (1804).

[44] J. Kielhorn, C. Melber, D. Keller, and I. Mangelsdorf, *Int. J. Hyg. Environ. Health* **205**, 417 (2002).

[45] S. Wang, J. Dougherty, W. Huebner, and J. Pepin, *J. Am. Ceram. Soc.* **77**, 3051 (1994).

[46] R. Rushforth, *Platinum Met. Rev.* **48** (2004).

[47] P. A. Crozier, R. Sharma, and A. K. Datye, *Microsc. Microanal.* **4**, 278 (1998).

[48] T. Ichinohe, S. Masaki, K. Uchida, S. Nozaki, and H. Morisaki, *Thin solid films* **466**, 27 (2004).

[49] T. Ichinohe, S. Masaki, K. Kawasaki, and H. Morisaki, *Thin solid films* **343-344**, 119 (1999).

[50] E. OWEN and E. YATES, *Phil. Mag.* **15**, 472 (1933).

[51] S.-W. LEE, Y.-C. JEON, and S.-K. JOO, *Appl. Phys. Lett.* **66**, 1671 (1995).

[52] Y. D. SEROPEGINA, A. V. GRIBANOVA, and O. I. BODAKB, *J. Alloys and Comp.* **269**, 157 (1998).

[53] E. VOOGT, A. MENS, O. GIJZEMAN, and J. GEUS, *Surf. Sci.* **350**, 21 (1996).

Chapter 4

Methodology

4.1 Transmission Electron Microscopy

Transmission Electron Microscopy (TEM) is a set of microscopy based techniques that are widely used to investigate the structure and properties of different types of materials. The main ingredient of these methods is an electron beam produced by high acceleration voltage that is focused onto a thin sample by means of electromagnetic lenses. The electrons interact strongly with the sample, creating diffracted beams of electrons, energy loss electrons, X-rays, back-scattered electrons, and secondary electrons. The transmitted electrons are then focused by electromagnetic lenses and imaged onto a fluorescent screen.

Scanning Transmission Electron Microscopy (STEM), Electron Energy Loss Spectroscopy (EELS), Energy Filtered Transmission Electron Microscopy - Spectral Imaging (EFTEM-SI), and Energy Dispersive Spectroscopy (EDS) were used to study the composition of the material systems investigated in this work, High Resolution Transmission Electron Microscopy(HRTEM) was used to study the atomic structure, and EELS was used to study the electronic structure. In the following sections, these techniques will be discussed in relation to the work presented in four papers.

4.1.1 Transmission Electron Microscopes

Two microscopes were used to study the nanoclusters in detail. The first microscope was a 200 keV JEOL 2010F microscope equipped with a Gatan imaging filter and detector. The spherical (C_s) and chromatic aberration (C_c) coefficients of the objective lens were 0.5 mm and 1.1 mm, respectively. The point to point resolution was 0.194 nm at Scherzer focus (-42 nm). A probe current of about 0.5 nA at a probe diameter of 1.0 nm can be obtained. The energy resolution at 200 keV can be about 0.8 eV.

The other microscope was a 300 keV JEOL 3100FEF microscope with an Omega energy filter. The spherical and chromatic aberration coefficients of the objective lens were 0.6 mm and 1.1 mm, respectively. The point to point resolution was 0.174 nm at Scherzer focus (-37 nm), and the minimum probe diameter was 0.2 nm. The energy resolution at 300 keV was 0.78 eV and was previously determined experimentally [1]. The energy dispersion of the Omega-filter was 0.85 μm/eV at 300 keV.

4.1.2 High Resolution Transmission Electron Microscopy

As silicon nanocrystals have low contrast when embedded in an SiO_2 matrix, it is difficult to observe them directly in bright field and dark field TEM images. It is, however, possible to distinguish the Si nanocrystals from the amorphous SiO_2 matrix by High Resolution Transmission Electron Microscopy (HRTEM) images showing Si lattice fringes. In papers 1, 3, and 4, this technique was applied to study the atomic structure of the nanocrystals and their environment in detail. HRTEM was performed using both the 300 keV JEOL 3100FEF TEM and the 200 keV JEOL 2010F TEM.

The main difference between conventional TEM and HRTEM is that HRTEM creates an image based on several beams, while conventional TEM produces an image from only one electron beam. The images in HRTEM are based upon the interference between the direct beam and the diffracted electron waves. Different materials give rise to slight phase differences in the wave function of the transmitted electron beams, creating contrast between different areas of the image. It should be remarked that in many cases this can be described by the weak phase object approximation. That is, it is considered that the sample is so thin that the amplitude variations

have only small effects upon the image [2, 3].

The Contrast Transfer Function (CTF) modulates the amplitudes and phases of the electron beams as they pass through the objective lens [2, 3]. It defines the point to point resolution and the information limit of the microscope. The CTF can be represented by

$$T(u) = -\sin\left(\frac{\pi}{2}C_s\lambda^3u^4 + \pi\Delta f\lambda u^2\right) \tag{4.1}$$

where λ is the electron wavelength, u is the spatial frequency, Δf is the defocus of the objective lens, and C_s is the spherical aberration coefficient.

The CTF of the JEOL 3100FEF microscope at Scherzer defocus (-37 nm) and at extended Scherzer defoucs (-44.4 nm) conditions are presented in Figure 4.1. Some important points to notice about this function are given below [2, 4]:

- CTF is oscillatory: there are "passbands" where it *is not* equal to zero (good "transmittance") and there are "gaps" where it *is* equal (or at least very close to) zero (no "transmittance").
- When it is negative, *positive phase contrast* occurs, meaning that atoms will appear dark on a bright background for thin samples (near the edge).
- When it is positive, *negative phase contrast* occurs, meaning that atoms will appear bright on a dark background for thin samples (near the edge).
- When it is equal to zero, there is no contrast (information transfer) for this spatial frequency.
- First crossing of the u-axis at Scherzer defocus corresponds to point-to-point resolution of the microscope.
- The point where the envelope functions (see below) damp the CTF to $1/e$ corresponds to the information limit of the microscope.

Other important features:

- CTF starts at 0 and decreases, then
- CTF stays almost constant and close to -1 (providing a broad band of good transmittance), then
- CTF starts to increase, and
- CTF crosses the u-axis, and then
- CTF repeatedly crosses the spatial frequency u-axis as u increases.
- CTF can continue forever, but, in reality, it is modified by envelope functions and eventually dies off. The effect of the envelope functions can be represented as

$$T(u)_{\text{eff}} = T(u)E_cE_a \tag{4.2}$$

where E_c is the temporal coherency envelope caused by chromatic aberrations, focal and energy spread, and instabilities in the high tension and objective lens current. E_a is the spatial coherency envelope (caused by the incident beam convergence) [2, 4].

Optical diffractograms are useful tools for detecting and correcting astigmatism and for determining the specimen movement during exposure, the focus of the recorded image, the microscopes spherical aberration constant, and the damping envelope constants due to chromatic aberrations, beam divergence and the focus and sample thickness [5, 6].

The focus conditions of the HRTEM images in paper 1 were found using a method developed by Thon et al. [6]. An optical diffractogram was made by Fast a Fourier Transform (FFT) of the HRTEM images.

The diffractograms showed several bright rings that represent the spatial frequencies that are optimally transferred by the objective lens [6]. The radial intensity of the ring pattern is approximately proportional to $\sin^2 \chi(u)$, where [5]

$$\chi(u) = \pi\lambda\Delta f u^2 + \frac{\pi}{2}\lambda^3 C_s u^4 \tag{4.3}$$

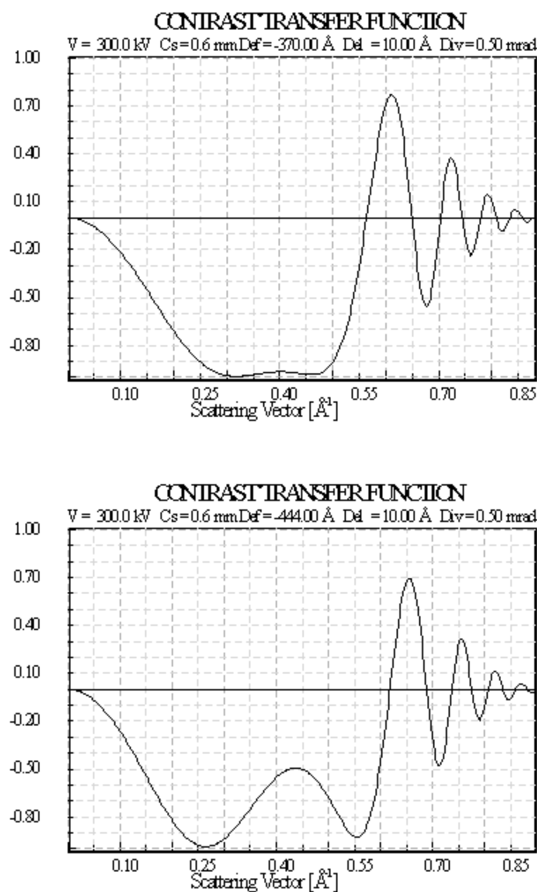

Figure 4.1: *The Contrast Transfer Function (CTF) of the JEOL 3100FEF. The top function is at Scherzer defocus (-37.0 nm), and the bottom function is at extended Scherzer defocus (-44.4 nm).*

Here λ is the electron wave length, u is the distance from the origin to the maxima and minima of $\sin^2\chi(u)$ in the optical diffractogram, C_s is the spherical aberration coefficient, Δf is the defocus of the objective lens, and $\sin\chi(u)$ is the transfer function representing the phase change due to defocusing and aberrations of the objective lens. The maxima (resp. minima) in the diffractograms correspond to $\sin^2\chi(u) = 1$ (resp. 0). These conditions are equivalent to $\chi(u) = n\frac{\pi}{2}$, with $n = 2k + 1$ is odd for maxima and $n = 2k$ is even for minima. For $\chi(u) = n$, Equation 4.3 can be transformed to

$$n/u^2 = 2\lambda\Delta f + (C_s\lambda^3)u^2 \tag{4.4}$$

This is a linear affine equation between $x = u^2$ and $y = n/u^2$ with slope $a = C_s\lambda^3$ that intersects the y-axis at $b = 2\lambda\Delta f$. For a given electron wave length and spherical aberration coefficient, the slope a can be calculated. The offset b can be used to find the focus of the experimental HRTEM image.

Plotting the expression $y = n/u^2$ as a function of $x = u^2$ yields a hyperbola for every fixed n, and the curves that were used in paper 1 are presented in Figure 4.2. Every distance u from the central beam to a maximum and minimum of $\sin^2\chi(u)$ in the experimental optical diffractograms should then satisfy the same linear relationship between $x = u^2$ and $y = n/u^2$ with slope $a = C_s\lambda^3$, but with different n.

It is unknown to which n a given distance u corresponds. One therefore draws a point on every hyperbola, keeping in mind that only one of these represents our data. Repeating this for every distance u, one arrives at a sequence of points for any u. As consecutive u correspond to consecutive n, fixing an n for the first u determines a sequence of points. One of these sequences should lie on the line given by Equation 4.4, and the sequence whose best fit has minimal error is the most likely candidate. The value $b = 2\lambda\Delta f$ was predicted by choosing this line.

The two straight lines in Figure 4.2 were calculated for two different HRTEM images in paper 1 according to the above process. The defocus Δf was then determined by the intersection $b = 2\lambda\Delta f$ of the straight line with the y-axis. Unfortunately, the measurements of the maxima and minima in the diffractograms have large standard deviations, yielding an accuracy of ± 10 nm in determining the Δf.

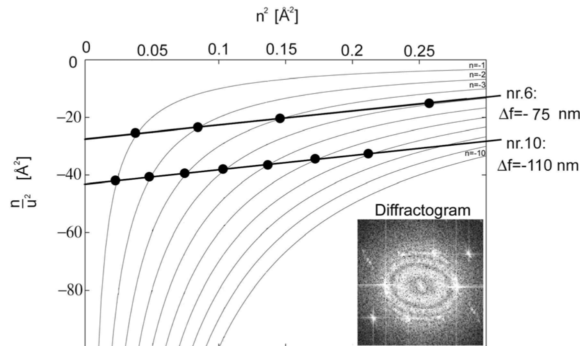

Figure 4.2: *A plot of n/u^2 as a function of u^2. The plot was used for finding the focus of the HRTEM images in paper 1. The image in the bottom right corner shows a diffractogram of HRTEM image no. 10 and a diffraction pattern from the Si-substrate in the same sample.*

HRTEM images of small unit cells may appear periodic with focus (Δf). The Fourier image period is the period for which the first and last HRTEM images are identical. The difference in focus of such images is given by Equation 4.5. The Fourier image period of HRTEM images can be computed from equation 4.5, for the strongest reflection u_{hkl} inside the objective aperture [7].

$$\Delta f = \frac{2}{\lambda u_{hkl}^2} \tag{4.5}$$

4.1.3 Energy Dispersive Spectroscopy

Energy Dispersive Spectroscopy (EDS) is an analytic technique used for elemental analysis and chemical characterization. In papers 3 and 4, this technique was applied to determine the composition in different layers in the samples. Quantitative EDS measurements were carried out using a 200 keV JEOL 2010F TEM with a NORAN system.

The EDS technique is based on the following process, depicted in Figure 4.3. Exposing the sample to an electron beam will cause some electrons to get kicked out of their shell, creating an electron core hole. In an attempt to minimize the energy of the atom, outer shell electrons will tumble down to fill these holes, emitting a photon in the process. Such high energy photons are called X-rays. The energy is equal to the difference in the energy before and after emitting the

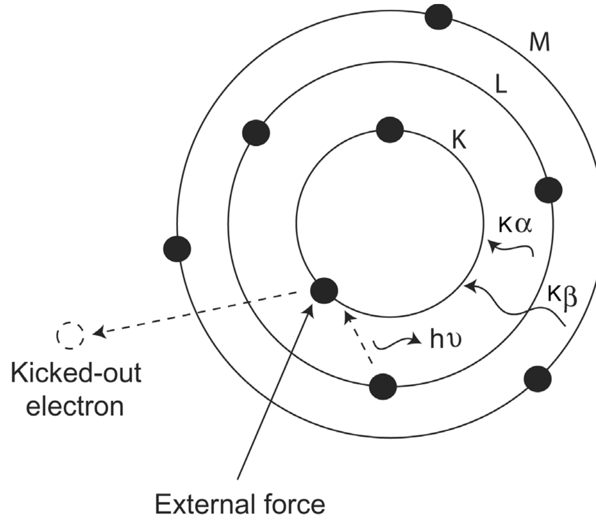

Figure 4.3: *The EDS process.*

photon. As such energy differences are characteristics of the elements, measuring the energy of the photons can be used to identify the elements present in the sample.

Technically, the emitted X-rays are detected and measured by a detector consisting of a Li doped Si crystal cooled to liquid nitrogen temperature.

The intensities of the peaks corresponding to the characteristic energies of the elements were used to determine the presence of different elements in the samples and to calculate the composition of the materials. According to Cliff and Lorimer [8], if I_i and I_j are the intensities corresponding to two elements i and j, the ratio of their compositions C_i and C_j is given by

$$\frac{C_i}{C_j} = k_{ij} \cdot \frac{I_i}{I_j} \tag{4.6}$$

The k_{ij} factors are called the Cliff-Lorimer k-factors. These vary from one detector to another, and they are independent of the specimen thickness, as long as the specimen is thin. In a thick specimen both the k-factor and the intensities of the X-rays are affected by absorption, fluorescence and channelling effects in the specimen [3, 4].

4.1.4 Electron Energy Loss Spectroscopy

Electron Energy Loss Spectroscopy (EELS) is a spectroscopy technique used to study the composition and electronic structure of materials. In paper 2, EELS was applied to study the plasmon energies of Si and SiO_2 and to determine the composition and electronic structure of the nanoclusters. Electron energy loss spectra were acquired with the JEOL 2010F microscope operated at 197 keV and equipped with a Gatan imaging filter and detector.

When the electron beam passes through the sample, some of the electrons will undergo inelastic scattering, which means that the kinetic energy is not conserved. The electrons have a loss in the kinetic energy and have slightly deflected paths, see Figure 4.4. The transmitted electrons pass through an imaging filter that measures the energy loss of these electrons [9].

Such inelastic interactions include phonon excitations, plasmon excitations, single electron excitations and direct radiation losses. Phonon excitations are atomic vibrations in the solid that raise the local temperature, and the energy losses due to them are very small, typically in the range 10-100 meV. These losses are therefore not easily resolved in the EELS spectrum available for the present work. Single electron excitations, on the other hand, were used for elemental analysis, as their energies are characteristic for the given element. Direct radiation losses or Bremstrahlung radiation is a result of deceleration processes of electrons in which energy is emitted directly in the form of photons. This radiation forms the background radiation in the EELS spectrum [10]. The different features present in the EELS spectrum of Si can be seen in Figure 4.5.

The most significant energy losses, however, are due to excitations of plasmons, which are collective, resonant oscillations of valence electrons in solids. Electrons can lose 5-30 eV by exciting plasmons and have a mean free path of 100 nm at 100keV. As this is usually short compared to the sample thickness, the plasmon scattering is the most frequent scattering process and the dominant feature in the EELS spectrum. The plasmon energy of the investigated materials was found experimentally, but they can also be calculated using the following equation [10].

$$E_p = \frac{h}{2\pi}\sqrt{Ne^2 m_e \varepsilon_0} \tag{4.7}$$

where N is the valence electron density, m_e the electron mass, ε_0 the permittivity of free space, h is Planck's constant and e the electron charge. The plasmon energy of Si is 16.8 eV, while the

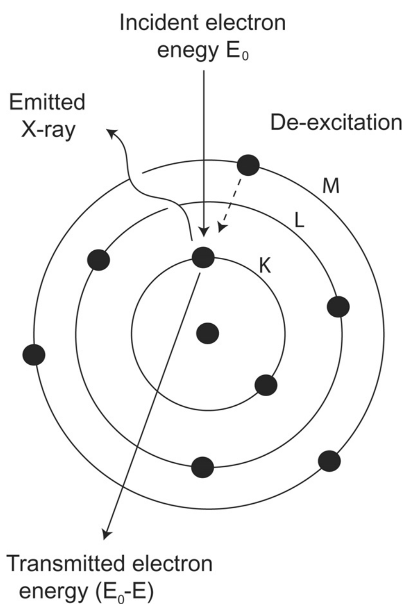

Figure 4.4: *De-excitation mechanism for an atom that has undergone K-shell ionization and subsequently emission of a characteristic Kβ X-ray.*

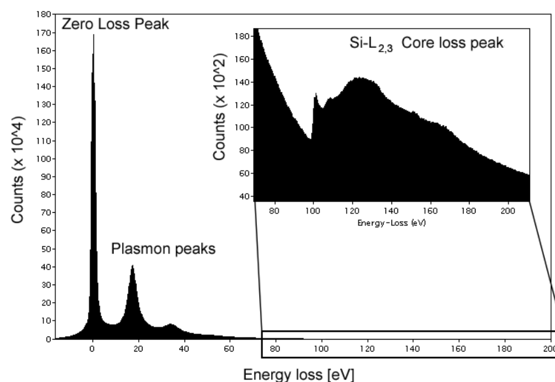

Figure 4.5: *An EELS spectrum of Si showing the different peaks present, with an energy dispersion of about 0.8 eV. The inserted EELS image has a lower count on the y-axis (10^2).*

corresponding value of SiO_2 is 23 eV. This is a 6.2 eV energy difference, which is large enough for the two peaks to be separated in the EELS spectrum. Shifts in the Si plasmon peak were studied in papers 1 and 2. This shift can be due to an increase in electron density or oxygen concentration, and this affects the shape of the plasmon peak.

4.1.5 Energy Filtered Transmission Electron Microscopy - Spectral Imaging

Energy Filtered Transmission Electron Microscopy - Spectral Imaging (EFTEM-SI) is a technique used in TEM to investigate the composition and electronic structure of materials. Applying EFTEM-SI yields both an EELS spectrum and an image with elemental information. Since the plasmon peak energy of Si is 16.8 eV and that of SiO_2 is 23 eV, EFTEM images using the plasmon peak of Si, and then of SiO_2, were obtained. Si nanoclusters have low contrast when embedded in an SiO_2 matrix. Therefore, crystalline Si nanoclusters were identified by lattice fringes, while the amorphous Si nanoclusters are not readily resolved by HRTEM. Paper 1 used EFTEM-SI to image the amorphous Si nanoclusters by imaging the plasmon peak of Si and extracting the crystalline Si nanocrystals from the HRTEM images. EFTEM imaging was carried out using both the JEOL 3100FEF and the JEOL 2010F microscope, while EFTEM-SI analysis

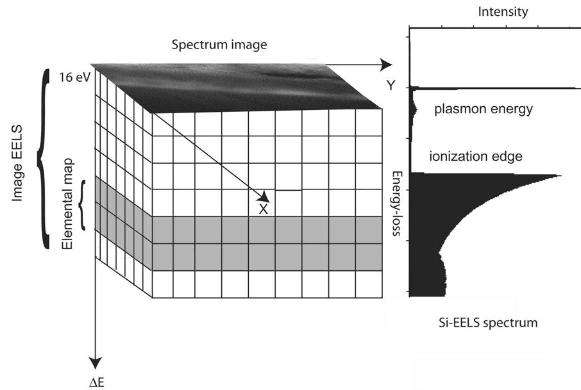

Figure 4.6: *The figure exhibits how an EFTEM-SI image is made up of an EELS spectrum in each point in the 2-dimensional image. The image at the top is made by the plasmon peak of Si, which lies at 16.8 eV. (Adapted from Ahn[11].)*

was performed using only the 300 keV JEOL 3100FEF TEM with an Omega imaging filter.

EFTEM images can be created from all the electrons with a particular kinetic energy. The other electrons are excluded by the presence of a narrow slit, and increasing the slit width will allow more electrons to be included in the image. By combining such EFTEM images for different energies in a certain energy range, one can create an EFTEM-SI file containing all the information of the individual EFTEM images in addition to the EELS spectra, see Figure 4.6.

4.1.6 Scanning Transmission Electron Microscopy

Scanning Transmission Electron Microscopy (STEM) is a TEM technique in which a focused electron beam is scanned over the sample. The STEM microscope has both a Bright Field (BF) detector and a High Angle Annular Detector (HAAD). With an HAAD, images with high Z-contrast can be obtained. In paper 4, STEM was used to image the Er distribution in the SiO_2-Si layers and the microscopy was performed using a 300 keV JEOL 3100FEF TEM equipped with an Omega imaging filter and a JEOL STEM detector.

The technique is based upon the fact that the Z-contrast is directly related to the atomic number (Z), making it possible to contrast materials with different atomic numbers. Atoms with a higher

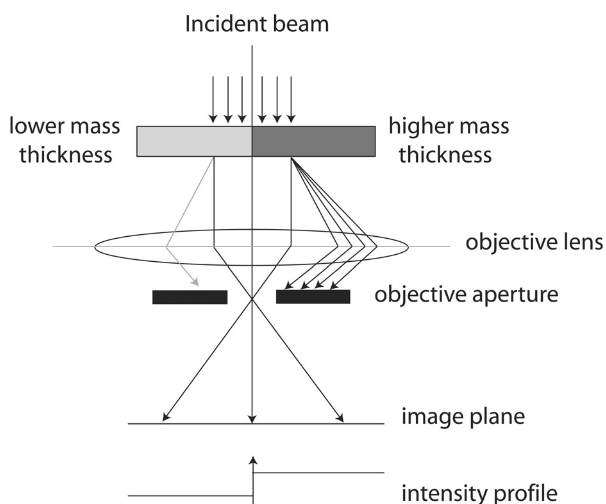

Figure 4.7: *The figure shows a sketch of Z-contrast/mass-thickness imaging. Thicker regions or regions with higher atomic number scatter more electrons off axes, causing them to show up as darker areas in the image. (Adapted from Williams and Carter [4].)*

atomic number have a more strongly charged electron cloud, repelling the trespassing electrons with more force. That is, the cross section of elastic scattering is positively correlated with the atomic number Z. Increasing the thickness of the specimen, on the other hand, will also increase the scattering angles, as long as the mean free path remains fixed.

After passing the sample and an objective lens, the electrons travel towards the objective aperture. Those electrons that have been scattered at large angles will not pass through this aperture, resulting in a difference in contrast between the parts with high-Z and low-Z [4], see Figure 4.7. This technique made it possible to detect Er-oxide in a SiO_2 matrix.

4.2 X-ray Photoelectron Spectroscopy

X-ray Photoelectron Spectroscopy (XPS) is commonly used as a surface analysis technique to characterize chemical states of surfaces and interfaces at shallow depths. It is also frequently used for studying the electronic structure of materials. XPS was used in papers 2, 3 and 4 to

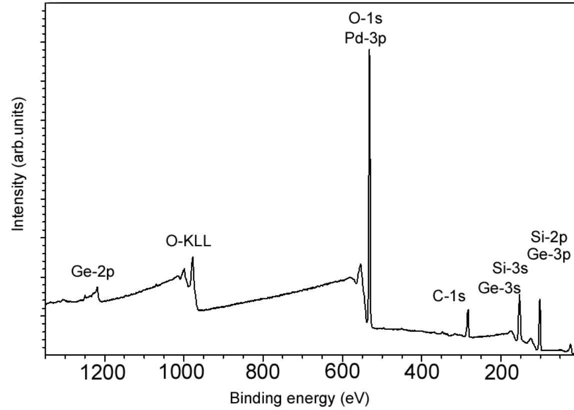

Figure 4.8: *A survey spectrum of the sample investigated in paper 4, containing Si, SiO_2, Ge, and Pd.*

study the composition of different layers present and the electronic structure of the nanoclusters in the material system. The XPS instrument used in paper 2 was a VG Scientific ESCALAB MKII with non-monocromatic Al Kα radiation on plane-view sample with a 45° take off angle. In papers 3 and 4 a KRATOS AXIS ULTRA^{DLD} XPS instrument was used with a monocromatic Al Kα radiation on plane-view samples using a 0° angle of emission (vertical emission). A survey spectrum of the Si-Ge-Pd sample investigated in paper 4 is presented in Figure 4.8.

In XPS, the sample is irradiated by an X-ray beam, causing electrons to eject from their atomic shells. When assumed that the process is elastic, the X-rays give rise to photoelectron emission according to Equation 4.8 [12]. Such electrons are called photoelectrons, and they are collected and analysed according to their energy by a spectrometer. The photoelectrons can only take energies in some discrete set of binding energies E_B that are characteristic for the electronic structure of the material. In the spectrometer these binding energies show up as XPS peaks, allowing one to identify the elements present in the sample. The Si-2p peak for the different oxidation states was extensively studied in paper 2, the Er-4d peaks in paper 3 and the Pd-3d peaks and Ge-3d peaks in paper 4.

$$E_K = h\nu - E_B - \phi \tag{4.8}$$

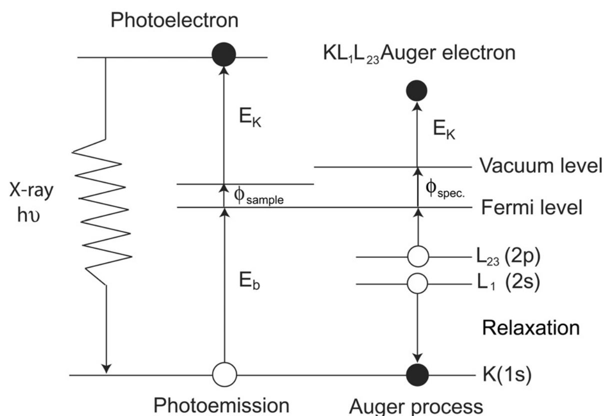

Figure 4.9: *The scattering process of a photon resulting in a photoelectron and an Auger electron. The figure is adapted from a book by Niemantsverdriet [13].*

In Equation 4.8, E_K is the kinetic energy of the photoelectron, $h\nu$ is the energy of the exciting radiation, E_B is the binding energy of the photoelectron with respect to the Fermi level of the spectrometer, and ϕ is the work function of the spectrometer. Equation 4.8 applies for conductors and semiconductors. In insulators the work function of the sample plays an important role. The work function will be discussed in more detail in Section 4.2.3.

In addition, there is a secondary effect that allows one to extract more information from the sample, depicted in Figure 4.9. Whenever a photoelectron is kicked out of its shell and leaves a vacancy behind in the excited atom, electrons from higher shells can fall down to fill up the hole, resulting in a release of energy. Sometimes this energy is released in the form of an emitted photon, and other times the energy can be transferred directly to another electron, which is then ejected from the atom. These secondary electrons are called Auger electrons, and their energies are characteristic for the sample as well. This effect and the use of the Auger peaks are explained in more detail in a later section.

4.2.1 Photoelectron escape depth

It should be remarked that XPS detects only those electrons that have actually escaped into the vacuum of the instrument, cutting out all electrons with energies below a certain threshold. The

probability of finding a particle at depth z into the material is calculated by Lambert-Beer's law

$$P(x) = e^{-z/\lambda} \tag{4.9}$$

where λ is the absorption length, which is the distance into the material corresponding to the situation of the probability that a particle has not been absorbed has dropped to $1/e$. The intensity of a beam of light measured before and after interaction with a sample is compared [14], and can therefore be described by as

$$I = I_0 e^{-\mu x} \tag{4.10}$$

where I_0 is the intensity of the incoming X-rays, x is the sample thickness and μ is the linear absorption coefficient. The flux of electrons emitted at a depth z and detected at a polar angle θ (see Figure 4.10) from the surface normal will be reduced by inelastic scattering according to the Beer-Lambert relationship [15] [16]

$$I(z, \phi) = I_0 e^{-z/(\lambda \sin \phi)} \tag{4.11}$$

where $I(z, \phi)$ is the intensity from the atoms at a depth z, I_0 is the intensity from the surface atoms, ϕ is the electron take-off angle ($\phi = 90 - \theta$, where θ is angle of emission), and λ is the mean free path. In the case of exponential decay, if the absorption length is λ_{AL}, then for a take-off angle ϕ to the surface, the escape depth d is equal to $\lambda_{AL} \sin \phi$. Commonly $3d$ (95 % detection) is taken to be the "sampling depth", which is equal to $3d\lambda_{AL} \sin \phi$ [16].

The mean free path of the elements of interest in this study were found using the NIST Standard Reference Database 71 [17]. The inelastic mean free path of a selected element in the database was determined by optical data and a theoretical model developed by Tanuma, Powell, and Penn [18]. This model is a modified form of the Bethe equation [19] for inelastic electron scattering in matter and is dependent of the atomic weight, bulk density, and number of valence electrons per atom, see Equation 4.12 [18].

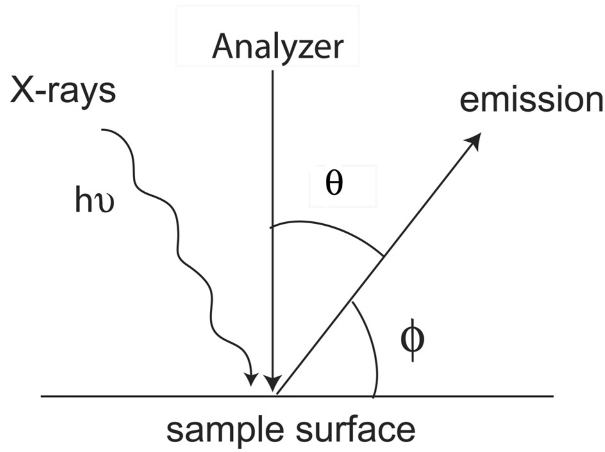

Figure 4.10: *The take-off angle ϕ and angle of emission θ.*

$$\lambda = \frac{E}{E_p^2[\beta \ln(\gamma E) - (C/E) + (D/E^2)]} \tag{4.12}$$

$$E_p = 28.8\sqrt{\frac{N_V \rho}{M}} \tag{4.13}$$

$$\beta = -0.0216 + \frac{0.944}{\sqrt{E_p^2 + E_g^2}} + 7.39 \cdot 10^{-4}\rho \tag{4.14}$$

$$\gamma = 0.191\rho^{-0.5} \tag{4.15}$$

$$C = 1.97 - 0.91U \tag{4.16}$$

$$D = 53.4 - 20.8U \tag{4.17}$$

$$U = \frac{N_v \rho}{M} = \frac{E_p^2}{829.4} \tag{4.18}$$

where E is the electron energy (in eV), E_p is the free-electron plasmon energy (in eV), N_v is the number of valence electrons per atom, ρ is the material density (in g/cm^3), M the atomic weight, and E_g the band-gap energy (in eV). The symbols γ, β, C, and D represent additional parameters.

4.2.2 The binding energy

The binding energy for a particular core level in a molecule (first approximation) can be expressed as Equation 4.19 [20]. This equation shows that the binding energies increase with increasing positive charge.

$$E_B = Kq + L \tag{4.19}$$

where K and L are empirical constants and q is the charge on the ion in the particular molecule relative to the neutral atom. Thus L is the binding energy of the electron in question in the free neutral atom.

In a molecule the electron experiences not only the charge of that atom, but will experience, apart from intra atomic relaxation, also extra atomic relaxation effects and potential charges from other atoms in the molecule. The relaxation energy R (intra- and extra atomic), is the energy gained when the electrons in the molecule respond to the photohole produced by the photoemission process. The relaxation energy is negative because it decreases the binding energy. The potential energy V produced by all other atoms in the molecule expresses the field produced by the charges of the other atoms. This leads to Equation 4.20.

$$E_B = Kq + V + L - R \tag{4.20}$$

4.2.3 The chemical shift

Shifts in the binding energy E_B were studied in paper 2, 3, and 4. Binding energy shifts are influenced by both initial (prior to photoemission) and final (after photoemission and Auger emission) state effects.

The chemical shift is the peak shift between two different chemical environments and is defined as the binding energy difference (ΔE_B) between atoms bonded to different chemical species, e.g. elemental Si and SiO_2 (E_B Si^{4+} - E_B Si^0). In pure Si, the 3p electrons form a band, and their wave function is therefore only partly at the site of a particular Si atom. However, in SiO_2 each Si atom donates its 3p electrons into the 2p shell of oxygen such that a closed $2p^6$ configuration is obtained. Thus in SiO_2 the Si 3p electrons have no part of their wave functions near the Si atom. The 2p electrons in SiO_2 feel a stronger Coulomb interaction than in pure Si, where the Si nucleus is shielded from the 2p shell through the 3p valence electrons. Therefore the binding energy of Si 2p level is larger in SiO_2 than in pure Si, and a chemical shift between the two compounds is observed.

This shift was used to help identify the different oxidation states of Si in paper 2, of Er in paper 3, and Pd and Ge in paper 4. However, determination of chemical shifts depends on reliable measurements of XPS peak positions, which in turn are sensitive to energy referencing issues. It is also difficult to compare samples that have been investigated with different spectrometers and/or experimental setups. When examining samples that are partially (semi)conducting and partially insulating, the sample surface tends to charge (non uniformly) when exposed to the X-ray beam. The non uniform charging creates different shifts in the XPS peaks, and this is called differential charging. Since the samples investigated in this work contained semiconducting nanocrystals in an insulating oxide, charging effects influenced the binding energies and therefore the chemical shifts. In papers 3 and 4 we used monochromatic radiation. Charging phenomena are more intense when monochromatic X-rays are used. However, the experiments were run using a charge neutralization system based on low kinetic energy electrons “flooding” the sample surface. When achromatic radiation is used (e.g. with a dual Al/Mg Kα anode) as in paper 2, charge compensation occurs to some extent by secondary electrons generated inside the spectrometer by the achromatic beam. Differential charging phenomena were studied in paper 2.

If final state relaxation effects are not taken into account, the core level binding energy difference between two compounds A and B is given by Equation 4.21 (after Equation 4.20).

$$\Delta E_B(A,B) = K(q^A - q^B) + (V^A - V^B) \tag{4.21}$$

The first term ($K\Delta q$) describes the difference in electron-electron interaction between the core orbital and the valence charges. It expresses the changes in the number of valence electrons in the atom. K is the Coulomb interaction between the valence and core electrons. The second term (ΔV) represents the interaction of the atom to be photoionized with the rest of the crystal and can be described by Equation 4.22 [21]

$$V_A \rightarrow \sum_{c \neq A}^{N} \frac{q_c}{r_{cA}} \tag{4.22}$$

where q_c is the effective charge on the set of atoms (except A) in the environment of A and the r_{cA} are the appropriate inter-atomic distances. In molecular solids the atoms A bonded to atom B, but in ionic solids the summation extends over the whole lattice. The r_{cA} terms in Equation 4.22 can be extracted from the lattice measurements or spectroscopic determinations, and only the effective charges q_c can be determined by any argument of the ionic character of the bond. This term is directly related to the Madelung energy of the solid and for this reason V is often referred to as the Madelung potential. The Madelung energy is described by Equation 4.23.

$$E = -\frac{Z^2 e^2 M}{4\pi\varepsilon_0 r_0} \tag{4.23}$$

where M is the Madelung constant, which is representative of the distance of the ions from one another in a specific type of crystal. It is described as the energy of a single ion, depending on how close it is to other ions and charges, and is a modified electron energy. $1/(4\pi\varepsilon_0)$ is the Coulomb force constant or the electrostatic constant equal to $8.987 \cdot 10^9$ Nm^2C^{-2}.

The two terms $K\Delta q$ and ΔV (in Equation 4.21) are initial state parameters and reflect changes in the atomic potential arising from changes in valence electron charge and Coulomb interactions at the emission site. In addition to these two terms, the chemical potential ($\Delta\mu$) or the work function (φ) are often added to the equation as energy referencing parameters [22]. The work function and the chemical potential are discussed in more detail in the next section. The chemical

shift can then be written in two ways,

$$\Delta E_B = K\Delta q + \Delta V + \Delta\varphi \tag{4.24}$$

and

$$\Delta E_B = K\Delta q + \Delta V + \Delta\mu \tag{4.25}$$

The effect of the relaxation on the chemical shift is not take into account in Equation 4.24 and 4.34 and will be discussed in Section 4.2.4.

4.2.4 Energy referencing, work function, and the chemical potential

In XPS, if the analyzed material is electrically conductive and in contact with the spectrometer material, then electrical equilibrium is achieved between the specimen and the spectrometer, i.e. their Fermi levels (E_F) are lined up, see Figure 4.9. It is convenient to assume for conducting specimens that the E_F of the spectrometer is zero in determining the kinetic energy of the ejected electrons. Electrons at the Fermi level are still bound to the metal, and have an ionization potential equal to the work function ϕ. Therefore, electrons coming from the Fermi level of the sample are detected with a kinetic energy equal to

$$E_K = h\nu - \phi_{sp} \tag{4.26}$$

where ϕ_{sp} is the work function of the spectrometer, and not that of the sample [13]. The binding energy is

$$E_B = h\nu - E_{kin} - \phi_{sp} \tag{4.27}$$

When the conducting sample gets in contact with the material of the spectrometer, their Fermi

levels are the same, but their work functions differ. In order to remove an electron at the Fermi level from the sample, energy costs equal to ϕ, the work function of the sample is used. Electrons will then pass from the metal with low ϕ to the metal with high ϕ. The electron that is liberated from the sample is now at the potential just outside the sample ("local vacuum level"), but not yet at the potential of the spectrometer, which in this set-up defines the vacuum level. While en $route$ to the analyzer, the electron is accelerated or decelerated by the work function difference, which is the contact potential between the sample and the spectrometer [13] until a potential difference $\phi_0 - \phi_{sp}$ is reached, where ϕ_0 is the work function of the sample. Since vacuum levels are different, it is necessary to add ϕ_0 to E_B in order to obtain ionization energies relative to the vacuum level.

$$E_{ion} = E_b + \phi_0 \tag{4.28}$$

So Equation 4.27 becomes

$$E_{ion} = h\nu - E_{kin} + (\phi_0 - \phi_{sp}) \tag{4.29}$$

If the specimen is a semiconductor (or insulator) then the Fermi levels are not equal. In addition, the electrical potential of the specimen and spectrometer are not equal (exceptions occur when thin insulating films are deposited on conducting substrates, then the potentials of the film and substrate even out). In this case

$$E_b = h\nu - E_{kin} - \phi_{sp} \pm E_{diff} \tag{4.30}$$

where E_{diff} is the difference between the potentials of the surface of the sample and the spectrometer. When we apply charge compensation, we flood electrons on to the sample surface so that the vacuum level of the sample now will be at the same level with the E_F of the spectrometer. Then

$$E_B = h\nu - E_K + Fe - \phi_{sample} \tag{4.31}$$

The work function can also be dependent on the chemical potential

$$\phi_{sp} = \Delta\phi_{met.} - \mu \tag{4.32}$$

where $\Delta\phi_{met.}$ is the rise in mean electrostatic potential across the metal surface, and μ is the bulk chemical potential of the electrons relative to the mean electrostatic potential in the metal interior.

The chemical potential governs the flow of particles between the system, just as the temperature governs the flow of energy [23].This means that when two systems with a single chemical species are at the same temperature and have the same value of the chemical potential, there will be no net flow and no net energy flow between them [23]. The chemical potential can be described as

$$\mu = \left(\frac{\partial U}{\partial N_i}\right)_{S,V,N_{j\neq i}} \tag{4.33}$$

where U is the internal energy of the system, V is the volume, S is the entropy, and the number of particles of each specimen is $N_1, \ldots, N_n$. The subscripts emphasize that the entropy, volume, and the other particle numbers are to be kept constant.

By taking into account final state relaxation effects, Equation 4.21 can be expressed as below, including the extra atomic relaxation energy.

$$\Delta E_B = K\Delta q + \Delta V + \Delta\varphi - \Delta R \tag{4.34}$$

If the experiment is performed in the same instrument, then the contribution of ϕ_{sp} in Equations 4.32 and 4.34 is zero. Assuming that ϕ_{sample} is the same in different chemical environments, Equation 4.34 can be simplified to

$$\Delta E_B = K\Delta q + \Delta V - \Delta R \tag{4.35}$$

The shift in kinetic energy can also be expressed in this matter, but has negative potential and positive relaxation energy terms.

$$\Delta E_K = -K\Delta q - \Delta V - \Delta\varphi + 3\Delta R \tag{4.36}$$

4.2.5 Screening

In the previous section we refered only to initial state effects in the binding energy shifts. However, binding energies are also influenced by changes in the extra atomic relaxation energy associated with changes in core hole screening. Since the chemical shift contains both initial and final state contributions, it makes it more difficult to determine the cause of the shift. In papers 2, 3 and 4, a core shift was found in the XPS peaks, and screening was discussed as a possible effect. The screening can be expressed by Equation 4.37. Two charges q_1 and q_2 separated by a distance r have a Coulomb interaction energy of

$$U(r) = \frac{k_e q_1 q_2}{r} \tag{4.37}$$

where $k_e = 1/(4\pi\epsilon_0) = 8.99 \cdot 10^9$ Nm^2/C^2 and ϵ_0 is the permittivity in vacuum or the electric constant. This equation expresses long range interactions because of its slow power-law decay.

The materials studied in this work have a high dielectric constant, 11.9 for Si, 16 for Ge, 13 for Er_2O_3, and 3.9 for SiO_2. The screening in a dielectric material can be described by the Coulomb interaction reduced in strength by the dielectric constant e, as seen in Equation 4.38. The reduction in Coulomb interaction is due to polarization of the particles in the dielectric material. Induced or permanent dipoles around a free charge will be oriented so as to terminate some of the field lines coming from the free charge. This effect is called the dielectric screening.

$$U(r) = \frac{k_e q_1 q_2}{er} \tag{4.38}$$

In papers 3 and 4, a core hole shift in the binding energy of Er-oxide and Pd was found. In order to determine the screening effect of the surrounding matrix on the clusters, the universal

"screening length" [24] was calculated for Er-oxide, Pd, Pd-oxide, and SiO_2. The universal screening length is expressed as

$$a_u = \frac{0.8854}{Z_1^{0.23} + Z_2^{0.23}} a_0 \tag{4.39}$$

where Z is the atomic number and a_0 is the Bohr radius ($52.9177 \cdot 10^{-3}$ nm).

4.2.6 Auger parameter

The initial (β) and final (α) state Auger parameters are important parameters to measure when investigating a material using XPS, and they are defined by Equation 4.40 and Equation 4.41.

$$\alpha = E_B + E_K \tag{4.40}$$

$$\beta = 3E_B + E_K \tag{4.41}$$

The α eliminates energy referencing problems [25] (see ΔE_B and ΔE_K in Equation 4.35 and 4.36) and was therefore used to identify chemical states of elements in the XPS spectrum.

The combination of Equations 4.34, 4.36, and 4.40 leads to two different expressions for Auger parameter changes reflecting either initial [26] ($\Delta\beta$) or final state [27, 28] ($\Delta\alpha$) effects.

$$\Delta\alpha = \Delta E_B + \Delta E_K = 2\Delta R \tag{4.42}$$

and

$$\Delta\beta = 3\Delta E_B + \Delta E_K = 2(k\Delta q + \Delta V + \Delta\varphi) \tag{4.43}$$

The final and initial state Auger parameter values calculated for the different samples investigated in paper 2 showed large deviations. Changes in the initial state Auger parameter showed that the shift in binding energy was mostly due to initial state effects, where the Si^0 sites in the nanoclusters had a negative charge, while the Si^0 sites in the supersaturated silica (with Si) had a positive charge.

Screening, being a final state effect, was also an important factor to consider. The final state Auger parameter is a measure of the screening efficiency in the presence of core holes and is free of any referencing problems [29, 30, 31]. Equation 4.42 shows how the final state Auger parameter provides an estimate of the relaxation/screening energy in the presence of core holes. It shows that a high α-value indicates higher relaxation energy or improved screening efficiency. It should be noted that Equation 4.42 is not reliable for transition metals, due to intra atomic charge transfer [32].

Due to the triple weighting of the binding energy E_B in its definition (see Equation 4.43), the initial state Auger parameter is not completely independent of energy referencing. Therefore, β can be potentially influenced by work function differences and charging effects. The initial state Auger parameter β reflects nevertheless changes in the population of valence electrons, as well as changes in the Madelung potential.

In order to visualize the initial and final state Auger parameter changes in paper 2, a Wagner diagram was plotted. A Wagner diagram [33] is made by plotting the binding energy of the photoelectron peak against the kinetic energy of the Auger electron peak. The Auger kinetic energy is on the ordinate and the photoelectron binding energy is on the abscissa oriented in the negative direction [25, 33]. The Wagner diagram plotted in paper 2 is shown in Figure 4.11. The Auger parameters are expressed by the linear relationship between E_K (Auger peak) and E_B (photoemission peak), and they lie on the straight lines with slope +1 (final state α) and +3 (initial state β). This means that for each line, every point lying on this line has the same Auger parameter value. This diagram helps to visualize changes in the relative Auger parameter values.

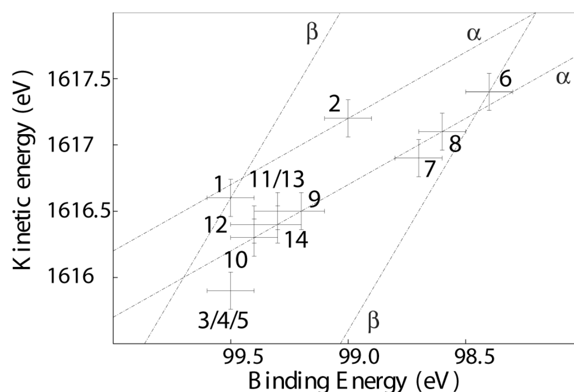

Figure 4.11: *A Wagner diagram plotted from the work in paper 1, of the samples with crystalline and amorphous Si nanoclusters.*

4.3 Secondary Ion Mass Spectrometry (SIMS)

Secondary Ion Mass Spectrometry (SIMS) is a composition analysis technique widely used to measure the concentration of doping elements in semiconductors. In paper 1 and 4, SIMS was used to determine the depth profile of Ge and Si in different layers.

A focused ion beam scans the surface, ejecting secondary ions that are collected and analyzed by a mass spectrometer. SIMS is a very sensitive technique and is able to detect elements in the parts per billion ranges. Cs^+ ions (15 keV) or O_2^+ ions (10 keV) are used to sputter depending on the elements in the sample which is to be analyzed. O_2^+ primary ions are often used to investigate electropositive elements, due to an increase in the generation probability of positive secondary ions. Cs^+ ions are often used when electronegative elements are being investigated. Therefore O_2^+ ions were used when extracting positive charged ions (Ge and Si).

The SIMS measurements were performed on a Cameca IMS 7f with a 25 nA O_2^+, 0.5 keV primary beam. After the SIMS measurements the depth of the craters were measured with a Dektak 8 stylus profilometer, for converting the sputter time to depth. The depth calibration was made on the assumption of a constant erosion rate.

References

[1] Y. Bando, M. Mitome, D. Golberg, Y. Kitami, K. Kurashima, T. Kaneyama, Y. Okura, and M. Naruse, *Jpn. J. Appl. Phys.* **40**, L 1193 (2001).

[2] HTTP://WWW.MAXSIDOROV.COM/CTFEXPLORER/WEBHELP/BACKGROUND.HTM.

[3] A. Olsen, *The Theory and Practice of Analytical Electron Microscopy in Material Science*, University of Oslo, 2002.

[4] D. B. Williams and C. B. Carter, *Transmission Electron Microscopy: A text book in Material Science*, Plenum press, New York, 1996.

[5] J. S. Spence, *Experimental High-Resolution Electron Microscopy*, Oxford University Press, 2 edition, 1988.

[6] F. Thon, *Electron microscopy in Material Science*, pp. 570–590, New York; Academic press, u. valdre and a. zichichi edition, 1971.

[7] A. Olsen and J. Spence, *Phil. Mag. A* **43**, 945 (1981).

[8] G. Cliff and G. Lorimer, *J. of Microscopy* **103**, 203 (1975).

[9] R. Egerton, *Electron Energy Loss Spectroscopy in the Electron Microscope*, Plenum press, New York, 1986.

[10] R. Brydson, *Electron Energy Loss Spectroscopy*, BIOS Scientific Publishers Limited, 2001.

[11] C. C. Ahn, *Transmission Electron Energy Loss Spectrometry in Materials Science and EELS ATLAS*, WILEY-VCH, 2 edition, 2004.

[12] D. Briggs and M.P.Seah, *Practical Surface Analysis*, volume 1, John Wiley ANd Sons AND Salle and Sauerlander, second edition, 1990.

[13] A. Dupasquier and A. P. Mills, *Positron Spectroscopy of Solids: Proceedings of the International School of Physics "Enrico Fermi", Varenna on Lake Como, Villa Monastero, 6-16 July 1993*, IOS Press, 1993.

[14] G. AKGUL, F. AKSOY, Y. UFUKTEPE, and J. LUNING, *Sol. Stat. Commun.* **149**, 384 (2009).

[15] F. BRUNO, L. FLOREANO, A. VERDINI, D. CVETKO, R. GOTTER, A. MORGANTE, M. CANEPA, and S. TERRENI, *J. Electron. Spectrosc. Relat. Phenom.* **127**, 85 (2002).

[16] D. BRIGGS, *Surface analysis of polymers by XPS and static SIMS*, Cambridge University Press, 1998.

[17] C. J. POWELL and A. JABLONSKI, *NIST Electron Inelastic-Mean-Free-Path Database 71*, National Institute of Standards and Technology, 2000.

[18] S. TANUMA, C. POWELL, and D. PENN, *Surf. Interface Anal.* **17**, 911 (1991).

[19] H. BETHE, *Ann. Phys.* **5**, 325 (1930).

[20] S. HÜFNER, *Photoelectron Spectroscopy: Principles and Applications*, Springer, 2003.

[21] T. L. BARR, *Modern ESCA: The Principles and Practice of X-ray Photoelectron Spectroscopy*, CRC Press, 1994.

[22] N. HARIMA, J. MATSUNO, A. FUJIMORI, Y. Y. ONOSE, TAGUCHI, and Y. TOKURA, *Phys. Rev. B* **64**, 220507 (2001).

[23] C. KITTEL and H. KROEMER, *Thermal Physics*, FREEMAN, 2 edition, 1980.

[24] S. TIAN, *J. Appl. Phys.* **93**, 5893 (2003).

[25] C. D. WAGNER, *Anal. Chem.* **47**, 1201 (1975).

[26] J. A. EVANS, A. LAINE, P. WEIGHMAN, J. A. D. MATTHEW, D. A. WOOLF, D. I. WESTWOOD, and R. H. WILLIAMS, *Phys. Rev. B* **46**, 1513 (1992).

[27] S. W. GAARENSTROM and N. WINOGRAD, *J. Chem. Phys.* **67**, 3500 (1977).

[28] T. D. THOMAS and P. WEIGHTMAN, *Phys. Rev. B* **33**, 5406 (1986).

[29] S. C. LAWRENCE, *J. Phys. Chem.* **55**, 95 (1971).

[30] C. G. H. WALKER, G. B. S. A. MOTRON, J. A. D. MATTHEW, and F. N. YOUSIF, *J. Electron. Spectrosc. Relat. Phenom.* **70**, 73 (1994).

[31] J. A. D. MATTHEW, S. A. MORTON, C. G. H. WALKER, and G. BEAMSON, *J. Phys. D* **28**, 1702 (1995).

[32] G. KLEIMAN and R. LANDERS, *J. Electron. Spectrosc. Relat. Phenom.* **76**, 319 (1995).

[33] G. MORETTI, *J. Electron. Spectrosc. Relat. Phenom.* **95**, 95 (1998).

Chapter 5

Sample preparation

Silicon is a brittle material, and the layers with nanocrystals were very thin. To image the different layers, cross-section samples were made, see Figure 5.1.

The samples were cut into two small rectangular pieces with a diamond tip pen. The samples were glued together with epoxy glue between two pieces of Si, in order to stabilize the TEM samples, see Figure 5.1. The epoxy glue has a transition temperature of 100°C with a degeneration temperature of 500°C. The epoxy is stable at a temperature up to 1000°C. The four pieces were then glued with crystal bond (which dissolves in Acetone) to a holding device and grounded thin with SiC papers of 300 to 1200 μm. When the samples had a thickness of 1 μm thin, they were glued to a Cu slot using epoxy.

To study the evolution of nanocrystal nucleation, in-situ heat treatment was performed on a sample with 70 area % Si described in paper 1. The experiment was done on a 300 keV JEOL 3100FEF microscope with an Omega image filter and a Gatan heating holder. The sample was heated up to 800°C, a temperature close to the melting point of Cu, at 1084°C. An Mo ring was therefore used instead (Mo has a melting point of 2623°C).

Thinning of the cross-sectional TEM samples were done by ion-milling using a Gatan precision ion-polishing system (PIPS) with twin argon-ion guns. The milling was operated at 5 kV gun voltage, with ion guns 7° from the top and 8° from below, relative to the specimen surface. The samples needed approximately 1.5 hours of milling to make a thin enough region for TEM

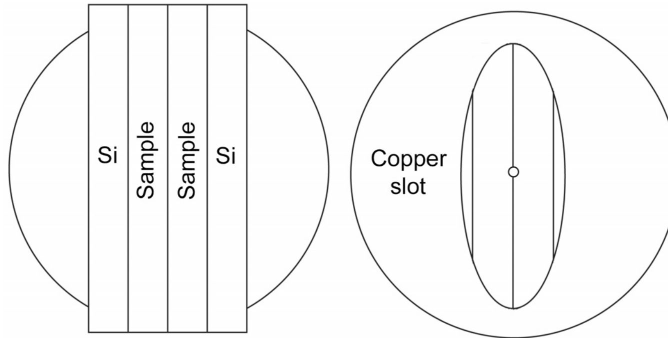

Figure 5.1: *A cross-sectional sample glued on a Cu slot.*

analysis.

The ion-gun angle relative to the specimen surface used in polishing these samples has to be higher than 6°. At lower angles Cu is sputtered from the Cu slot onto the samples. Cu nanoclusters were then formed in the SiO_2 layer, see Figure 5.2. This figure is from a sample that should only contain Si nanocrystals in a SiO_2 matrix. At first glance, these clusters might be taken to be Si nanoclusters, but Si has very low contrast compared to the SiO_2. Therefore the nanoclusters cannot be Si clusters. An EDS analysis showed high amounts of Cu, which confirms that they are Cu clusters originating from the Cu slot. Since high ion-gun angles were used when preparing samples for the in-situ heat-treatment, no Mo were observed in the heat-treated samples.

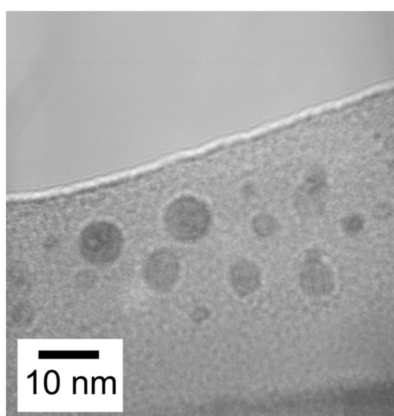

Figure 5.2: *Cu nanoclusters in SiO_2, introduced during surface preparation with too small grazing incidence angle of the sputter beam in the ion etcher.*

Chapter 6

Overview of papers

This work is presented in four papers and is in cooperation with the Physical Electronics group at MINAlab, where Jeyanthinath Mayandi made the samples with Terje Finstad as his supervisor. Part of the work was also done during a four month stay at the National Institute of Material Science (NIMS) in Tsukuba Japan, with Masanori Mitome and Yoshio Bando. The two first papers have been published in Journal of Applied Physics, the third has been submitted and the last paper will be submitted shortly as of this writing.

Paper I

In the previous chapters, the memory device stability was discussed with regards to the atomic structure and size of the nanoclusters, nucleation, distribution, and defects. Several samples containing pure Si embedded in a thin SiO_2 layer, heat treated at different temperatures and times, were studied by HRTEM, EDS, EELS, EFTEM, and SIMS. Jens Sherman Christensen ran the SIMS measurements on the instrument at MINAlab.

The study revealed both amorphous and crystalline nanoclusters of Si in the amorphous SiO_2 matrix. At low Si percentage (below 50 area %) only amorphous Si nanoclusters were nucleated in the oxide, and at higher Si concentration, crystalline nanoclusters were observed. TEM and SIMS results showed that the nanocluster nucleation occurred where maximum excess Si is the highest: in a 4 nm band, 5 nm from the Si substrate, and 4 nm from the SiO_2 surface.

Defects (twins and stacking faults) in the nanocrystals were also found and studied in detail by HRTEM and image simulations. Both single and double twin boundaries were observed in the nanocrystals.

Paper II

As discussed in the previous sections, the atomic and electronic structure can have large effects upon the material properties. To obtain a better understanding of the electronic structure of the nanoclusters observed in paper 1, an XPS study of the binding energy and the Auger parameter of the different samples were performed. EELS was used to study the shift in plasmon energy of the different samples and in order to relate it to the valence electron density.

The XPS study was under the supervision of Spyros Diplas, who ran the XPS measurements at the instrument in Surrey England, and John F. Watts contributed with comments and discussions.

The XPS results of the amorphous and crystalline nanoclusters showed large shifts in binding energy and Auger parameter. The shift in Si_{2p} binding energy was studied by separating initial and final state effects using the Auger parameter. The negative charge on the Si^0 sites in nanoclusters and the positive charge on the Si^0 sites in the supersaturated silica, as indicated by the initial state Auger parameter, dominated both differential charging and chemical shifts. The differences in chemical shift was attributed to initial state effects. The final state Auger parameter showed that the electron screening of silicon core holes in nanocrystals dispersed in SiO_2 is inferior to that in pure bulk Si. This is due to the non local screening character of Si.

Paper III

In this paper samples containing Er with only small amounts of pure Si in the SiO_2 matrix were investigated by HRTEM, EFTEM-SI, EELS, STEM, and XPS in order to study the effect on nucleation, distribution, and composition.

Amorphous Er-oxide nanoclusters were observed. These nanoclusters nucleated as a result of electron beam exposure. The nanocluster evolution was studied in detail. Initially the nanoclusters' growth matched the Ostwald ripening model, but eventually it stagnated at a constant nan-

ocluster radius of 2.4 nm. The nanocluster composition was studied by microscopy techniques and XPS to be Er-oxide, probably Er_2O_3. XPS spectra of the Er-4d peak showed an increase in binding energy. This may be attributed to initial state effects dominated by increased charge transfer from Er towards O in the presence of Si at the nanocluster-SiO_2 matrix interface.

Paper IV

As discussed previously, Ge is an interesting material for use in memory storage materials. Multilayer samples with both pure Si and pure Ge were made in order to study both Si and Ge nanocrystals. Martin F. Sunding ran the XPS measurements on the XPS machine at MINAlab.

During sputtering deposition, the samples were contaminated with Pd, creating an interesting type of diffusing Pd nanocrystals in the oxide. An extensive study of the nanocluster formation and their distribution, atomic and electronic structure, and the diffusion mechanisms were studied by HRTEM, EFTEM, EDS, and SIMS. The SIMS measurements of the different elements in the sample were performed by Lasse Vines at the MINAlab. The samples contained Pd nanocrystals and Ge and Si nanoclusters. The as deposited samples also contained PdO and PdSi compounds. The Pd nanocrystals diffused in the oxide when exposed to the electron beam and could be controlled by the electron beams location, intensity, and spot size. The diffusion was due to an increased vibration and fluctuation in the nanocrystals when being exposed to the electron beam, as well as due to the effect of charging of the nearby Ge and Si nanoclusters and the vacancy creation. Core hole shift in the Pd-3d peaks studied by XPS was due to initial state effects such as an increase in electrostatic potential in the nanocrystals.

Paper I

A. Thogersen, J. Mayandi, T. Finstad,
J. S. Christensen, M. Mitome, Y. Bando and A. Olsen
Characterization of amorphous and crystalline silicon nanoclusters in an ultrathin silica layer.
Journal of Applied Physics **74**, 245109 (2008)

Paper II

A. Thogersen, S. Diplas,
J. Mayandi, T. Finstad, J. F. Watts
M. Mitome, Y. Bando and A. Olsen
An experimental study of charge distribution in crystalline
and amorphous Si nanoclusters in thin silica films
Journal of Applied Physics **70**, 195119 (2008)

Paper III

A. Thogersen, J. Mayandi, T. Finstad
S. Diplas, M. Mitome, Y. Bando and A. Olsen
The formation of Er-oxide nanoclusters in SiO_2
thin films with excess Si
Submittes to Journal of Applied Physics (2009)

Paper IV

A. Thogersen, J. Mayandi, L. Vines, M. F. Sunding
T. Finstad, S. Diplas, M. Mitome, Y. Bando and A. Olsen

Composition and electron beam assisted diffusion study of Pd- and Ge-containing nanoclusters in a SiO_2 matrix.

Will be submitted to Journal of Applied Physics shortly

List of Abbreviations

ROM	Read Only Memories
NNMD	Nonerasable Nonvolatile Memory Devices
PROM	Programmable Read Only Memories
MROM	Mask Read Only Memories
EPROM	Erasable Programmed Read Only Memories
OTPM	One-Time Programmable Memories
EEPROM	Electrically Erasable Programmable Read Only Memories
USB	Universal Serial Bus
CMOS	Complementary-Metal-Oxide-Semiconductor
MOS	Metal-Oxide-Semiconductor
HRTEM	High Resolution Transmission Electron Microscopy
TEM	Transmission Electron Microscopy
EDS	Electron Dispersive Spectroscopy
EFTEM-SI	Energy Filtered Transmission Electron Microscopy - Spectral Imaging
EFTEM	Energy Filtered Transmission Electron Microscopy
EELS	Electron Energy Loss Spectroscopy
CTF	Contrast Transfer Function
FFT	Fast Fourier Transform
STEM	Scanning Transmission Electron Microscopy
HAAD	High Angle Annular Detector
BF	Bright Field
XPS	X-ray Photoelectron Spectroscopy
AP	Auger Parameter
SIMS	Secondary Ion Mass Spectrometry
PDA	Personal Digital Assistant

RTO	Rapid Thermal Oxidation
FCC	Face Centred Cubic
HCP	Hexagonal Closed Packed
BCC	Body Centred Cubic
RCA	Radio Corporation of America
PGM	Platinum Group Metals
GM	Granular Metal